Master Thesis

Manufacturing of thin film solid electrolyte Lithium Lanthanum Titanium Oxide (LLTO) through radio frequency magnetron sputtering

carried out at

Institute of Chemical Technologies and Analytics
Technische Universität Wien

under the supervision of

Univ.Prof. Dipl.-Phys. Dr.rer.nat. Jürgen Fleig
Univ.Ass. Dipl.-Ing. Dr.rer.nat. Andreas Nenning, BSc
Projektass.(FWF) Dipl.-Ing. Joseph Ring, BSc

by

Nicole Rosza, BSc

December 2022, Vienna

Abstract

Lithium lanthanum titanium oxide (LLTO) and lithium phosphorus oxynitride (LIPON) are two representatives of solid electrolytes (SE) for use in all-solid-state lithium-ion batteries (ASSLiB). LLTO has a perovskite structure with relatively high ionic conductivity at room temperature. However, the material is unstable in contact with metallic lithium. LIPON, on the other hand, has sufficient stability against lithium but does not exhibit high ionic conductivity values.

In this thesis, LLTO and LIPON sputter targets are fabricated and thin films are prepared in a radio frequency (RF) magnetron sputtering machine.

Structural identification of the sintered sputter targets is done by X-ray diffraction (XRD) measurements. Phase pure and compact LLTO pellets are obtained with a sintering temperature of 1100 °C, a heating ramp of 10 °Cmin^{-1} and a sintering time of 8 h. Corresponding LIPON targets are manufactured with a sintering temperature of 750 °C, a temperature holding step at 500 °C and a sintering time of 8 h.

In the course of the sputtering experiments, LLTO thin films are successfully produced. The thin films are analyzed by inductively coupled plasma–mass spectrometry (ICP-MS), XRD, atomic force microscopy (AFM), scanning electron microscopy (SEM) and electrochemical impedance spectroscopy (EIS). In addition, the film thicknesses are measured with a profilometer.

The stoichiometry of the thin films is determined with ICP-MS measurements. The results show that the ratio of lithium to lanthanum in the films is much lower than in the powder. The samples have predominantly smooth surfaces with no major defects and film thicknesses in the range of 150 nm to 300 nm. Crystalline films are obtained by hot sputtering at temperatures above 350 °C. The impedance measurements indicate the presence of electronic conductivity in the thin film samples.

Kurzfassung

Lithium Lanthan Titan Oxid (LLTO) und Lithium Phosphor Oxynitrid (LIPON) sind zwei Vertreter von Festkörperelektrolyten (SE) für die Anwendung in Lithium-Ionen Feststoffbatterien (ASSLiB). LLTO weist eine perowskitische Struktur und eine hohe ionische Leitfähigkeiten bei Raumtemperatur auf. Das Material ist jedoch instabil in Kontakt mit metallischem Lithium. LIPON hingegen besitzt eine ausreichende Stabilität gegen Lithium, kommt aber nicht an die ionische Leitfähigkeit von LLTO heran.

In dieser Arbeit werden LLTO und LIPON Sputtertargets hergestellt. Entsprechende Dünnfilme werden in einer Radiofrequenz (RF) Magnetron Sputter Maschine produziert.

Die strukturelle Identifizierung der gesinterten Sputtertargets erfolgt über Röntgenbeugungsmessungen (XRD). Phasenreine und kompakte LLTO Targets werden mit einer Sintertemperatur von 1100 °C, einer Heizrampe von 10 °Cmin^{-1} und einer Sinterzeit von 8 h erhalten. Entsprechende LIPON Targets werden mit einer Sintertemperatur von 750 °C, einem Temperaturhalteschritt bei 500 °C und einer Sinterzeit von 8 h produziert.

Im Zuge der Sputterexperimente konnten LLTO Dünnfilme erfolgreich hergestellt werden. Die Dünnfilme werden mit den Techniken der induktiv gekoppelten Plasma-Massenspektrometrie (ICP-MS), Rasterkraftmikroskopie (AFM), XRD, Rasterelektronenmikroskopie (SEM) und elektrochemischer Impedanzspektroskopie (EIS) analysiert. Zusätzlich werden die Filmdicken mit einem Profilometer gemessen.

Die Stöchiometrie der Dünnfilme wird mit ICP-MS Messungen ermittelt. Dabei zeigt sich, dass das Verhältnis von Lithium zu Lanthan in den Filmen um einiges geringer als im Pulver ist. Die Proben weisen überwiegend glatte Oberflächen mit keinen großen Defekten und Filmdicken im Bereich von 150 nm zu 300 nm auf. Kristalline Filme werden durch Heißsputtern bei Temperaturen über 350 °C erhalten. Die Impedanzmessungen zeigen das Vorliegen von elektronischer Leitfähigkeit in den Dünnfilmproben an.

Danksagung

Mein großer Dank gilt Prof. Dr.rer.nat Jürgen Fleig, in dessen Forschungsgruppe ich meine Diplomarbeit durchführen durfte.

Persönlich danke ich meinen beiden Betreuern Joseph Ring und Andreas Nenning, die stets mit Rat und Tat zur Seite standen. Josephs immerwährender Optimismus und Andreas' Hilfe bei der Analyse von Impedanzspektren und Erklärung seltsamer Sputtereffekte waren eine große Stütze.

Weiters möchte ich mich bei der gesamten Arbeitsgruppe für das tolle Arbeitsklima und deren Unterstützung bedanken. Besonders hervorheben möchte ich Tobias Huber, der für den Bau der Sputteranlage, dem Kernstück meiner Arbeit, maßgeblich beteiligt war.

Im näheren Arbeitsumfeld möchte ich meine Bürokollegen Andreas Bumberger und Florian Kubik nennen. Florians moralische Unterstützung während der Diplomarbeit war eine große Stütze, ohne ihn hätte sich die Arbeit um einiges mühsamer und langwieriger gestaltet. Unsere Bastelnachmittage werden mir ewig in Erinnerung bleiben.

Abschließend möchte ich mich bei meinen Freunden und meiner Familie für die Unterstützung durch ihre Herzenswärme während des gesamten Studiums bedanken.

Contents

Chapter 1

Introduction

In today's world, the energy demand is as high as never before. Energy sources based on fossil fuels have to be replaced as there is limited availability and their combustion leads to severe environmental damages including global warming. Therefore, there is the aim to increase the fraction of renewable energy sources. Various forms exist including solar, wind, geothermal or hydropower energy. However, renewable energy sources have the drawback that their operation mode is dependent on space and time. This factor, together with growing energy consumption and the non-evenly distributed consumption of electric energy, is contributing to the demand for effective (electric) energy storage (EES) facilities. Energy storage converts one form of energy into another, which will be stored and fed into the power grid when required. Various principles, including mechanical, thermal, chemical, electrical and electrochemical storage, can be applied. The prerequisites are aimed at environmentally friendly, efficient and versatile storage possibilities. [1–3]

EES can be distinguished by their properties including cost, lifetime, power density and energy density. These properties further determine the field of application.[4] Electrochemical and electromagnetic storage devices, such as batteries or supercapacitors, are highly used in zero-emission vehicles or portable electronic devices. Batteries are a form of electrochemical energy conversion as chemical energy is converted into electrical energy. [2, 3, 5]

The transport sector is responsible for a substantial part of the global CO_2 emission through the combustion of fossil fuels. The aim is to decarbonize this sector, where rechargeable batteries can play a central role. One important battery property is the energy density, a parameter which describes the amount of storable energy, based on the weight or volume of a battery. Another parameter is the lifetime, which specifies the feasible number of cycles upon charging and discharging. [6] The "power density refers to how quickly a device can discharge its energy". [7] Currently, lithium-ion batteries are the dominant application form. [6]

Generally, lithium batteries can be divided into two classes, primary and secondary batteries. The former uses metallic lithium as an anode material and is not rechargeable. Lithium-ion batteries (LiBs) are secondary batteries and rechargeable. Herein, intercalation materials are both used for the anode and cathode. The choice of the electrode materials and the electrolytes is very important because they influence the battery properties due to their structure and electrochemical behaviour. [8, 9] Lithium-ion batteries are very efficient energy storage devices as they offer a wide range of advantages. They exhibit "high open-circuit voltage, large discharge capacity, long cycle life and environmental friendliness". [9]

The chemical nature of lithium metal determines the unique characteristics of this battery type. Lithium displays the lowest reduction potential (-3.04 V vs. standard hydrogen electrode) among all elements, which allows a high cell potential in Li-based devices. Furthermore, lithium possesses a high theoretical capacity (3860 $\mathrm{mAhg^{-1}}$). Due to the small size of lithium-ions, high volumetric and gravimetric capacitance as well as a high power density can be achieved. Nevertheless, the use of metallic lithium as an anode material holds two major disadvantages. Firstly, lithium dendrites are formed during battery cycling which affects the overall safety due to the threat of arising short circuits. Secondly, the dendrite growth reduces the coulombic efficiency which has a detrimental effect on the lifetime. [10, 11] Solid electrolytes may overcome this issue.

1.1 Fundamentals of lithium-ion batteries

A lithium-ion battery consists of three main parts, the anode, the cathode and the electrolyte. Both electrodes are intercalation materials, where lithium-ions can be stored and relocated within the structure. Furthermore, the electrodes have to be separated by a membrane, which is only permeable to lithium-ions. Herein, short circuits are prevented. The cathode can consist of a metal oxide with a layered or tunnelled structure. An example of the former is lithium cobalt dioxide which does show good electrochemical properties but is less suitable for common applications due to cost and safety issues.
The anode can consist of alloying, insertion-type or conversion-type materials. Carbonaceous materials like graphite layers are widely used and belong to insertion-type materials. The formation of lithium dendrites can be prevented which enhances the safety factor. However, this material class has a limited gravimetric and volumetric capacity.
Common electrolyte systems contain dissolved lithium salts in organic solvents. Electrolytes are required to be good ionic and poor electronic conductors. [2, 6, 9, 12]

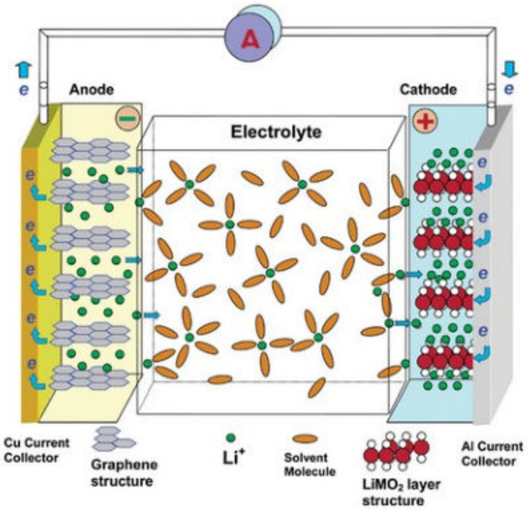

Figure 1.1: Schematic drawing of a lithium-ion battery with graphene anode, liquid electrolyte and LiMO$_2$ cathode. Reprinted with permission from [13]

A schematic drawing of a lithium-ion battery is displayed in Figure 1.1

Upon charging, lithium-ions deintercalate from the cathode oxide material and migrate to the anode, where they intercalate into the anodic layers. Simultaneously, electrons are transported over an external circuit from the cathode to the anode to guarantee charge neutrality. These mechanisms are reversed in the discharging cycle.[14] Within the cycling process of a LiB, a solid electrolyte interface (SEI) is formed between the anode and the electrolyte. This interface is crucial for the rechargeability property as it prevents the further reduction of the electrolyte through the reduction potential of the anode. The SEI has to be lithium-ion but not electronically conductive, and has the meaning of an additional interface which reduces the power density. [15, 16]

Despite the advantages, LiBs do also have considerable disadvantages where further optimization work is required. Although the energy density of LiBs has increased strongly over the past decades, it is still not sufficient for application in heavy vehicles.[6] Furthermore, LiBs exhibit a decreasing battery capacity throughout cycling. [17] Additionally, liquid electrolytes pose a safety hazard due to their thermal instability and the risk of leakages. [18]

Next-generation applications include sodium-ion batteries, redox-flow batteries or solid-state batteries, where the latter will be discussed in more detail. Herein, metallic lithium could be installed as an anode material due to the use of a solid electrolyte. The electrolyte has to display high ionic conductivities and sufficient contact with the electrode material. In general, solid-state batteries can lead to a safer application form and increased energy densities. [6]

1.2 Introduction to all-solid-state lithium-ion batteries

One strategy to overcome the safety concerns of standard LiBs is the implementation of all-solid-state lithium-ion batteries (ASSLiBs) where solid electrolytes (SE) are used. ASSLiBs exhibit a broad range of advantages. The substitution of liquid electrolytes has solved a major safety problem as organic liquids are highly flammable. The energy density can be increased by using higher potential cathodes and by reduction of dead weight through a more compact battery design.[19] In principle, it is also possible to use metallic lithium as an anode material which would additionally increase the energy density. Moreover, stiff electrolytes could prevent the growth of dendrites of lithium metal during battery cycling. [20]

Nevertheless, the main problems within ASSLiBs are referred to the electrolyte ionic conductivity and the solid-solid interfaces. For the latter, sufficient contact between the electrode and electrolyte is required. Otherwise, the internal resistance increases, leading to deterioration in cycling behaviour and power performance. [21, 22]

1.3 Aim of the thesis

This thesis aims to research solid electrolytes which can be used in ASSLiBs. Herein, the attention lies on the sputtering of thin film solid electrolytes with radio frequency (RF) magnetron sputtering. Sputter targets are manufactured from scratch.
The electrolytes lithium lanthanum titanium oxide (LLTO) and lithium phosphorus oxynitride (LIPON) are chosen for the work due to their reported beneficial properties. LLTO displays a high ionic conductivity for a solid electrolyte. The conductivity of LIPON is lower, but this material is chemically stable in contact with metallic lithium, which is a desirable property in ASSLiBs. [19, 23]

The novelty within this thesis is the target manufacturing process and the subsequent sputtering on thin films. The major challenge is the chemical and electrochemical characterization of the sputtered thin film samples. Small film thicknesses limit the measurement possibilities. In addition, elemental lithium can not be analyzed with various techniques due to its electronic configuration.

Chapter 2

Theoretical Background

2.1 Fundamentals of thin film solid lithium-ion batteries

Due to the rapid development of the electronic sector, the demand for microbatteries is constantly increasing. Herein, the use of downscaled bulk-sized LiBs, which consist of liquid electrolytes and composite electrodes, is not possible because of the requirements for the microfabrication process. Microbatteries are made of thin layers of active electrode materials and solid electrolytes, where the thicknesses of these films are limited. For electrodes, the avoidance of power loss is aimed. Additionally, the thickness reduction leads to smaller diffusion lengths, which are beneficial for a fast equilibrium setting. The problem of lower ionic conductivity can be diminished by using thin film electrolytes. A smaller layer thickness leads to a reduced internal resistance, which has a positive effect on the rate capability. The internal resistance can be expressed as the sum of the bulk ionic conductivity and the ionic transport through the electrolyte-electrode interface. Moreover, a higher gravimetric energy density is obtained by reducing the weight of the battery.
Thin film batteries show high thermal stability and are better rechargeable than batteries containing liquid electrolytes. However, thin film batteries are not suitable for high-power applications due to their limited energy which is caused by the reduced film thickness of the electrode materials. [8, 24–26]

The balance between miniaturization and the demand for good energy properties is a crucial point in the manufacturing process. Current thin film batteries use LIPON as an electrolyte, although materials with much higher ion conductivity like LLTO are known. Therefore, optimization work regarding the cell geometry and material choices is required. Moreover, the morphology of the thin film solid electrolytes plays an important role as structural defects can lead to short-circuits. Various techniques can be used for the production of thin film solid electrolytes, including radio frequency (RF) magnetron sputtering or pulsed laser deposition (PLD). [23, 27, 28]

2.2 Introduction to solid electrolytes

Solid electrolytes must meet certain requirements: The electronic conductivity has to be low in contrast to the ionic conductivity to prevent self-discharge and short-circuits. Sufficient chemical, thermal and electrochemical stability has to be guaranteed and the material should ideally be non-toxic. [27]

The major challenges within solid electrolytes lie in the demanded ionic conductivity and stability in contact with electrode materials. Liquid electrolytes have a high ionic conductivity in the range of 10^{-3} to $10^{-2}\,\mathrm{S cm^{-1}}$, but the Li-ion transference number is low due to the mobility of the counter-ion (typically $\mathrm{PF_6}^-$).[23, 29]
The transference number is a major parameter in battery systems. This number indicates how much of the total amount of electric current is transported by one type of charge carrier in an electrolyte. Lithium-ions are responsible for charge transport in LiBs where large power densities are better achievable with a high transference number. [27]
Solid electrolytes, on the other hand, have a transference number of one but lower ionic conductivities, realistic conductivity values are in an area of $10^{-4}\,\mathrm{S cm^{-1}}$. Various materials have been studied that have the necessary conductivity, but these are often unstable. This can include hygroscopic behaviour or lacking stability in contact with the electrode material. [23]

Two main material groups can be used as solid electrolytes, organic polymers and inorganic ceramics. Polymers possess low elastic moduli which favour an application in a flexible battery construct. Furthermore, they are often easier to fabricate, which lowers the cost. In contrast, ceramics are of a more rigid structure. They can be used in thin film batteries and high-temperature applications. [30]

The ionic conductivity of inorganic ceramic electrolytes (mainly sulfide, phosphate or oxide materials) arises from the movement of ionic point defects. This movement is thermally activated which is leading to increased conductivity at high temperatures. In some cases, ceramic electrolytes exhibit high ionic conductivities even at room temperature. [30]

Phosphate-based electrolytes can display good lithium-ion conducting properties. The amorphous electrolyte lithium phosphorous oxynitride (LIPON) belongs to this group, but its ionic conductivity is in the low 10^{-5} to $10^{-6}\,\mathrm{S cm^{-1}}$ range. [30] Nonetheless, this material is popular in microbatteries due to its large electrochemical stability window. [19]

Three important structure groups can be assigned to oxide solid electrolytes, namely garnet materials, lithium super ionic conductors (LISICON) and perovskite materials. [27] In comparison to sulfide electrolytes, oxide materials stand out due to their "high electrochemical stability ($> 8\,\mathrm{V}$), a good chemical/structural stability in a dry or humid atmosphere and a wide operating temperature range." [31] However, the main disadvantage is their rather low ionic conductivity. This property is influenced by grain boundaries in the crystalline lattice where the migration of ions can be blocked. Another important factor is the interface to the electrode material since the stiffness of the electrolyte does not always guarantee sufficient mechanical contact. [27]

Garnet electrolytes have the general formula of $\mathrm{Li_7Ln_3M_2O_{12}}$, with transition metals for M atoms and lanthanides for Ln atoms. The cubic phase can be stabilized through doping, which increases ionic conductivity. Nevertheless, they react sensibly to moisture in the environment and exhibit high resistance in contact with metallic lithium.
LISICON structures have lower conductivities at room temperature in comparison to other electrolyte materials. The ionic conductivity can be increased through a replacement of oxygen with sulphur. [27]
Perovskite materials have highly reported bulk conductivities, whereas the total conductivity is lowered due to grain boundary effects. The material has the formula of $\mathrm{ABO_3}$ and forms stable phases at different temperatures. One promising example of this structure class is lithium lanthanum titanium oxide (LLTO). [32]

2.3 Fundamentals of lithium lanthanum titanium oxide

It has been reported that the perovskite-type oxide electrolyte $\mathrm{Li_{3x}La_{2/3-x}TiO_3}$, lithium lanthanum titanium oxide (LLTO), exhibits high ionic conductivities at room temperature in the range of $10^{-3}\,\mathrm{Scm^{-1}}$. [23] Furthermore, LLTO is chemically and thermally stable in contact with air, has a large lithium-ion transference number and is electrochemically stable over a wide range. [33] However, the grain boundary resistance lowers the ionic conductivity to values below $10^{-4}\,\mathrm{Scm^{-1}}$. [23] Reported ionic conductivity values for amorphous LLTO are in the region of $10^{-5}\,\mathrm{Scm^{-1}}$. [34] Another disadvantage of crystalline LLTO is its instability against lithium metal. At potentials lower than 1.8 V, $\mathrm{Ti^{4+}}$ gets reduced to $\mathrm{Ti^{3+}}$ due to intercalation of lithium, thus leading to electronic conductivity. [23, 35] Moreover, the brittle structure of the material hampers the manufacturing process. [33]

LLTO crystallizes in the perovskite structure ABO_3, where “Li^+ and La^{3+} share the A-sites (coordination number = 12), and Ti^{4+} generally occupies the B-sites (coordination number = 6)“. [31] Titanium ions are octahedrally coordinated by oxygen atoms. In addition to the lithium and lanthanum ions vacancies are present on the A-sites. [31, 33] The crystal structure is displayed in Figure 2.1.

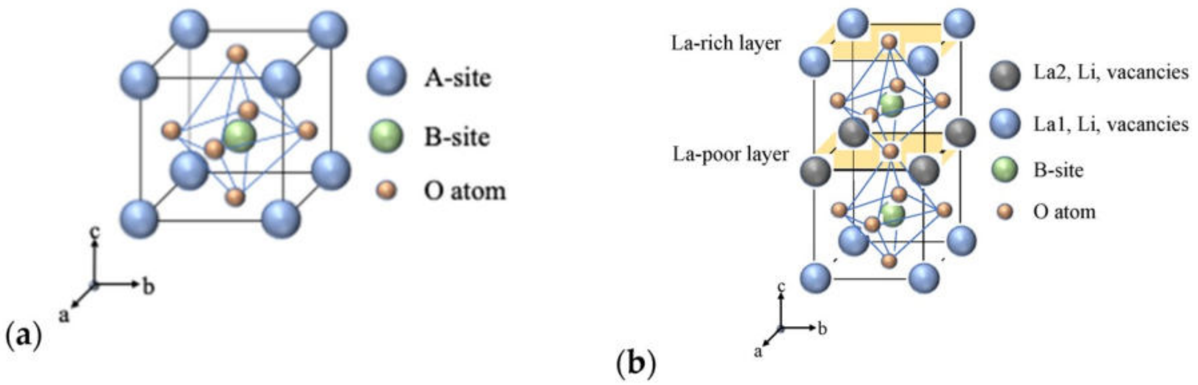

Figure 2.1: Figure a: general perovskite structure, for LLTO: A-site atoms: La, Li, B-site atoms: Ti; Figure b: stacked structure of LLTO with La-poor and La-rich layers. Reprinted with permission from [36].

Dependent on the chemical composition and due to the unequal distribution of the A-sites cations and vacancies, various distorted structures can arise. Generally, stable perovskite structures are maintained within a range of $0.04 < x < 0.16$. The lattice structure can be influenced by the sintering temperature. Tetragonal and cubic phases form a lattice with La-rich and La-poor layers. The stacking occurs along the c-axis where the transport of lithium-ions is favoured in the lanthanum-deficient layers. This disordered structure and the presence of vacancies enable lithium-ion conductivity. Nevertheless, grain boundaries between the lanthanum layers can act as a bottleneck because the transport of lithium-ions in lanthanum-poor layers is blocked at the boundary to lanthanum-rich layers. There is an optimum concentration value of x = 0.1 regarding the conductivity behaviour. The ionic conductivity depends on the ratio of vacancies to lithium-ions. Although there is an optimal value, grain boundary effects lower the ionic conductivity. [31, 33]

Various factors influence the transformation of the space group during manufacturing, including molar composition and heating/cooling behaviour. Compositions with a low lithium content, $0.03 < x < 0.1$, exhibit an orthorhombic lattice, whereas lithium-rich phases, $0.1 < x < 0.167$, crystallize in a tetragonal form. During heating, a phase transformation from the cubic to the tetragonal phase occurs. Furthermore, the cooling rate affects the crystallization process. Slow cooling rather leads to an orthorhombic structure, and quenching results in a rhomboidal lattice. This is due to the change from an ordered La-layer structure at lower temperatures to a more disordered structure at higher temperatures. Upon a fast cooling process, the disordered structure manifests. [37]

The largest drawback of LLTO is its low ionic conductivity due to high grain boundary resistance. One way to reduce this resistance is the insertion of dopant atoms on A-sites respectively B-sites because point defects are created. An amorphous structure does also enhance ionic conductivity because of the disordered structure where grain boundaries do not play a major part. Furthermore, the interface between electrolyte and electrode is more stable upon cycling. Such amorphous films can be produced by various techniques, including PLD and RF magnetron sputtering. In sputtering, crystalline films are formed upon temperatures higher than 400 °C. [23, 33] There is also the option to perform an annealing step after film deposition. Herein, the arrangement of atoms gets facilitated which lowers the number of defects in the film. [38]

2.4 Fundamentals of lithium phosphorus oxynitride

Lithium phosphorous oxynitride (LIPON) is an amorphous solid electrolyte. It displays various advantages in comparison to other lithium-based solid electrolytes including stability against lithium metal, overall chemical and electrochemical stability and good cyclability in battery applications. The general formula is described with the term $\mathrm{Li_{2y+3z-5}PO_yN_z}$. The properties of the material, like the ionic conductivity, can be adjusted through stoichiometry tuning over the sputtering parameters. Sputtering with nitrogen gas leads to the incorporation and cross-linking of nitrogen atoms in the phosphate groups of the sputtered film, which increases the ionic conductivity. The challenges within the RF magnetron sputtering process lie in the required high vacuum surrounding and the inert gas atmosphere. [19, 27, 39, 40]

The incorporation of nitrogen atoms in the lithium phosphate film can be divided into three steps. Firstly, the bonding of nitrogen atoms in the gas is split due to the plasma power, and nitrogen cations and electrons are formed. These cations can be incorporated into the film in the second step. Finally, the adsorption of nitrogen takes place and oxygen gets removed from the structure. [39] Incorporating nitrogen increases the ionic conductivity and the stability of the sputtered film. This is achieved through the reconstruction of phosphate chains in the structure. Nevertheless, an increasing nitrogen content leads to a smaller lithium fraction, which reduces the ionic conductivity. [41]

In the literature, it is stated that the insertion of nitrogen leads to double and triple bonds with phosphorus. However, new studies were carried out where no clear evidence for triply coordinated nitrogen atoms was found, instead "apical nitrogen in isolated $P(O,N)_4$ tetrahedra as well as bridges between two phosphate groups" were identified. [39] The structure is illustrated in Figure 2.2

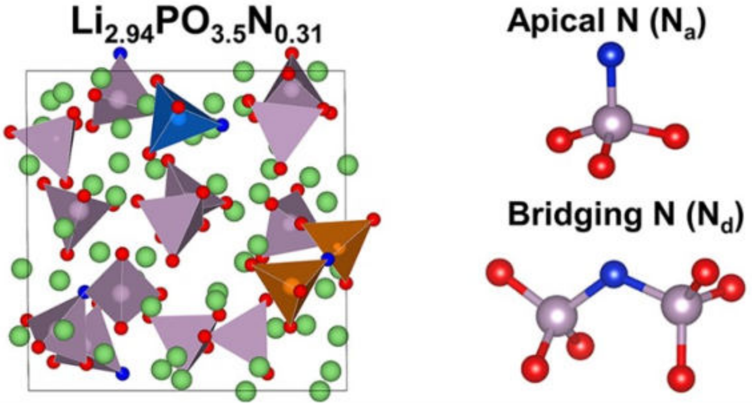

Figure 2.2: Left image: general structure of LIPON, red atoms: oxygen, blue atoms: nitrogen, green atoms: lithium, grey atoms: phosphorus. Right image: two nitrogen configurations within the structure. Reprinted with permission from [42].

The increase in ionic conductivity is attributed to the energy raise of lithium sites in the lattice. Herein, disordered phosphorus polyhedra in the amorphous structure are affecting the energy state of lithium sites, caused by enhanced lithium-ion mobility. Nitrogen bridges in the lattice „lower the electrostatic interaction between Li^+ and anions. By decreasing the interaction between lithium-ions and the anions, the ionic conductivity is improved." [39]

Generally, the Li/P ratio can be used to describe ionic conductivity. Likewise, the N/P ratio affects this property as it has been shown that the ionic conductivity increases with decreasing Li/P and increasing N/P ratio. Within incorporation, 1.3 oxygen atoms are replaced with 1.0 nitrogen atoms, simultaneously a single lithium atom is removed from the lattice. [39]

The overall ionic conductivity is in the range of $10^{-6}\,Scm^{-1}$. This makes the material to a candidate for thin film batteries, but not for bulk applications, where LIPON is a highly used electrolyte in the former. Herein, the film thickness is a crucial parameter because a layer of several hundred nanometers would lead to high cell resistance. A downscaling of the thickness is necessary, which has further a beneficial effect on the energy density. [41]

2.5 Principles of radio frequency magnetron sputtering

Magnetron sputtering belongs to the group of physical vapour deposition (PVD) techniques. Herein, thin films are generated in a vacuum chamber upon the atomization or vaporization of a target material. [43]

The basic mechanism of magnetron sputtering can be described as followed. A target material is bombarded by high-energy ions. These ions are formed upon a glow-discharge plasma from inert gas atoms in the sputter chamber. Through the collision of the ions onto the target's surface, target atoms get removed. The target atoms are deposited on a substrate and film growth occurs. The film has ideally the same stoichiometry as the target material itself. The collision of the ions also causes the emission of secondary electrons of the target material which are important for the preservation of the plasma. The use of magnets has brought a significant improvement in the sputtering process as deposition rate and ionisation efficiency increase. Magnets are placed behind the target in a way that one pole is formed in the middle of the target, and the other one is located at the edge and has a circular form through the ring arrangement of the magnets. Through the generated magnetic field especially electrons get attracted along the magnetic flux lines. The attraction of electrons is most effective at the region where the magnetic lines lie parallel to the target's surface. This zone is called the race track zone where an increased sputtering happens. In this region, a dense plasma is formed which increases the ionisation efficiency and thus the deposition rate. The properties of the sputtered film depend on the plasma power and the pressure inside the sputter chamber. [44–46]

In RF magnetron sputtering an alternating electric field is used, usually with a frequency of 13.56 MHz. This method allows the use of non-conductive targets. Otherwise, charging processes would occur which would affect the film deposition. The drawback of RF magnetron sputtering is the low deposition rate and the expensive setup. [44, 45] A schematic illustration of the RF magnetron sputtering process is illustrated in Figure 2.3.

The main challenge within sputtering lithium compounds is the arising lithium loss during sputter deposition. This loss has several reasons including the "low lithium sputter yield from the target, loss of lithium species during the gas phase transport, and low rate of lithium incorporation into the growing film due to resputtering or a low sticking coefficient". [47] Furthermore, lithium is highly mobile due to its low molecular weight which can cause a rapid removal of the target's surface. [47]

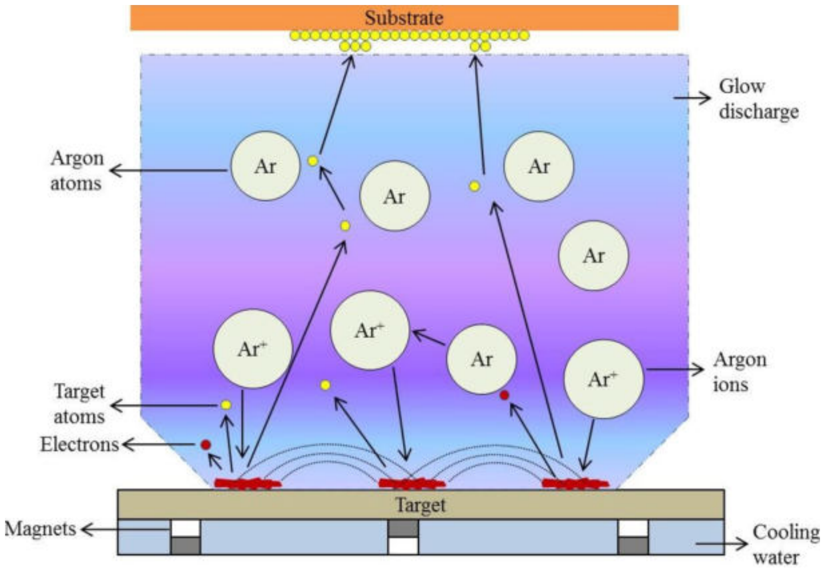

Figure 2.3: Schematic of RF magnetron sputtering process with indicated race track zones through magnetic flux lines; the maximum of sputter deposition takes place between the red areas at the target's surface. Reprinted with permission from [45].

2.6 Introduction to electrochemical impedance spectroscopy

Electrochemical impedance spectroscopy (EIS) is a useful characterization method for electrochemical systems due to its relatively simple measurement setup. Furthermore, physical properties can be obtained through data fitting with designed models. [48]

For impedance measurements, a sinusoidal potential with a small amplitude is applied to an electrochemical cell, Equation 2.1. The current response gets recorded, which is a sinusoid at the same frequency but with a phase shift compared to the excitation signal, Equation 2.2. The impedance can be expressed with Equation 2.3, which is a frequency-dependent resistance. To record an impedance spectrum, a scan over the frequency range with the excitation potential is performed.
In the equations, E_0 respectively I_0 are the amplitudes of the voltage/current signal, ω is the radial frequency (Hz), ϕ the phase shift (°) and t the time (s). [49–52]

$$E_t = E_0 \cdot \sin(\omega t) \tag{2.1}$$

$$I_t = I_0 \cdot \sin(\omega t + \phi) \tag{2.2}$$

$$Z = \frac{E_t}{I_t} = \frac{E_0 \cdot \sin(\omega t)}{I_0 \cdot \sin(\omega t + \phi)} = Z_0 \frac{\sin(\omega t)}{\sin(\omega t + \phi)} \tag{2.3}$$

Through the use of Euler's relationship, the impedance can be displayed as a complex number, Equation 2.4.

$$Z = \frac{E_t}{I_t} = Z_0 \cdot exp(\cos(\phi) + j \cdot \sin(\phi)) \tag{2.4}$$

However, the interpretation of the data has to be carried out thoughtfully. It is often the case that several models would fit the experimental data, making the analysis ambiguous. [48]

In an electrochemical cell, which consists of electrodes and an electrolyte, various processes, such as mass/charge transfer or diffusion, can take place. These processes, together with the characteristics of the single components, can influence the electrochemical cell properties, such as conductance, resistance or capacitance. With impedance spectroscopy, these effects can be observed and interpreted. [50]
The concept of resistance is described as the "ability of a circuit element to resist the flow of electrical current". [49] In Ohm's law, the resistance is defined over the voltage-to-current ratio where no frequency dependency is present. [49]

Electrical circuit components can be characterized by their phase shift behaviour. A resistor displays no phase shift and is described purely by the real part of impedance, Equation 2.5. The impedance of an inductor, Equation 2.6, and capacitor, Equation 2.11, is expressed only by the imaginary part. An inductor has a phase angle of + 90°, whereas a capacitor has a phase angle of -90°. [52] However, a capacitor is often modelled with a constant phase element (CPE), which expresses its non-ideal behaviour under real conditions, Equation 2.8. The capacitance can then be calculated with Equation 2.9. The exponent n refers to the non-ideal behaviour and is 1 for an ideal capacitor. [50, 53]

$$Z = R \tag{2.5}$$

$$Z = j\omega L \tag{2.6}$$

$$Z = \frac{1}{j\omega C} \tag{2.7}$$

$$Z = \frac{1}{(j\omega)^n Q} \tag{2.8}$$

$$C = (R^{1-n}Q)^{\frac{1}{n}} \tag{2.9}$$

The Bode diagram and the Nyquist plot are two common forms of impedance data visualization, the latter will be explained in more detail. In the Nyquist plot, the negative imaginary part of the impedance is plotted against the real part of the impedance. Every data point corresponds to one frequency value. In typical setups, high-frequency features appear on the left side of the plot. [49] The shape of a Nyquist plot depends on the electrochemical processes which occur in an electrochemical system. The formation of a double-layer capacitance at an electrode interface or the resistance of an electrolyte are two examples, where the former can be described with a capacitor and the latter with a resistor. Equivalent circuits (EC) can be designed, which consist of different electrical components (resistor, capacitor, inductor) and are used to model impedance data. Fitting the data allows a better interpretation of conductivity, reaction kinetics and dielectric properties. Furthermore, material properties like ionic conductivity can be calculated when using the parameters received from the fit. [50]

A common EC model is an RC circuit, which consists of a resistor connected in parallel with a capacitor, the capacitor can be replaced with a CPE. The impedance response of the circuit appears as a semicircle in the Nyquist plot. The EC can be used for the description of a solid electrolyte. A modified circuit is displayed in Figure 2.4. Herein, a resistor (R1), which represents the resistance of the cables, and a CPE (CPE2), which models the ion-blocking electrode, are added. Ion-blocking electrodes, such as platinum or gold, block the ions at the electrode interface and an additional interface is formed.

The ionic conductivity behaviour of crystalline materials can be divided into two parts, the bulk resistance and the resistance arising at the grain boundaries. Therefore, two semicircles are expected. The fitting of the plot is, however, not trivial as the two semicircles often merge into each other. [54]

The ionic conductivity of an electrolyte can be calculated using the following formula, Equation 2.10. Herein, σ is the ionic conductivity ($\mathrm{S\,cm^{-1}}$), d the electrolyte thickness

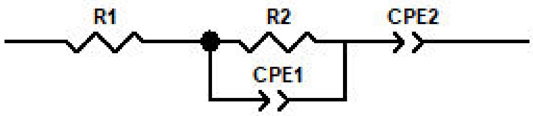

Figure 2.4: Equivalent circuit for a solid electrolyte (R2/CPE1) in an ion-blocking electrode configuration (CPE2) with an additional offset through cables (R1); CPEs are used for the modelling of a non-ideal behaviour.

(cm), A the area of the contacting electrode (cm^2) and R the resistance (Ω), where the latter can be obtained from the parameter of the corresponding EC fit. [55]

$$\sigma = \frac{d}{AR} \tag{2.10}$$

The capacitance of a plate capacitor can be calculated with Equation 2.11. Herein, C is the capacitance (F), ϵ_r the relative permittivity (Fm^{-1}) and ϵ_0 the permittivity of free space (Fm^{-1}). [56]

$$C = \epsilon_r \epsilon_0 \frac{A}{d} \tag{2.11}$$

Chapter 3

Experimental

3.1 Target manufacturing process

3.1.1 LLTO targets

Targets with a diameter of 2.54 cm were produced for the sputtering process. The LLTO powder (weight composition lithium 1.1 wt%, lanthanum 45.0 wt%, titanium 26.0 wt%, $Li_{0.3}La_{0.59}TiO_3$, TOHO TITANIUM CO., LTD.) was mixed in a mortar with press wax, one to two wt% of the powder mass were used for the wax. The powder was pressed to a pellet with a uniaxial press (P/O/Weber Modell 10, Gr. III). A working pressure of usually 260 bar and a pressing time of one minute were applied. It could occur that the pellet exhibited cracks after the pressing step. Herein, the pellet was finely ground in a mortar and pressed again.

The pellets were sintered in a corundum crucible in a furnace (Nabertherm N7 with temperature controller TR1). The pellet was covered with LLTO powder to minimize lithium loss during sintering. Different sintering programs were carried out. The goal was to find a program which resulted in a flat and dense pellet where no phase transformation took place and which could be identified as LLTO.

A summary of the produced LLTO targets, including sintering time and sintering temperature, heating ramp and applied pressure (the press time was always one minute), is given in Table 3.1. Furthermore, the optical appearance is described. The targets often showed little pores/cavities on the surface.

The last step of the target manufacturing process was the bonding of the sintered pellet to a copper plate with a thickness of about 3 mm (E-Cu, diameter 25 mm, product code 2.0060). The surface of the pellet and the copper plate was ground beforehand with abra-

Table 3.1: Manufacturing conditions of LLTO targets

sample	time (h)	temperature (°C)	heating ramp (°Cmin^{-1})	pressure (bar)	appearance
15.04	48	1050	-	173	flat, little cavities
24.05	8	1100	-	260	flat, little cavities
07.06	8	1100	-	260	flat, no pores
18.07	8	1100	10	260	flat, no pores
04.08	8	1100	10	260	flat, no pores
05.09	8	1100	10	347	flat, no pores
08.09	8	1100	10	260	flat, little cavities on the edge

sive paper to improve bonding quality. A high-temperature epoxy resin (Duralco 4700 adhesive epoxy) was used for bonding, consisting of a resin and a hardener, where 100 parts of the the resin were mixed with 28 parts of the hardener by weight. This mixture was homogenized until a black paste was formed. The copper plate was thinly coated with the paste, then the pellet was pressed against it. The bonded target was thermally cured in three steps with the following procedure. A first hardening step was carried out at 120 °C for 4 h. Then the target was cured at 175 °C for 2 h and finally at 230 °C for 16 h.
Annotation: For the first targets a fine steel mesh was used as a spacer between the copper plate and target to improve the thermal conductivity. However, this practice resulted in uneven targets.

For the structural characterisation, X-Ray Diffraction (XRD) measurements were performed on an X'Pert MPDII (Philips) device with Cu-K$_\alpha$ radiation (45 kV, 40 mA) in Bragg Brentano geometry. The diffractograms were compared to the XRD database and the positions of the reflexes were analyzed to investigate alterations of the unit cell.

The targets were further analyzed with X-ray fluorescence (XRF), Raman, laser ablation-inductively coupled plasma–mass spectrometry (LA-ICP-MS) and inductively coupled plasma–mass spectrometry (ICP-MS) measurements.

Raman measurements were conducted with an Alpha 300 RSA (WITec) device using a laser excitation wavelength of 531.959 nm and a laser power of 10.009 mW.

The XRF analysis took place on an Axios advanced spectrometer (PANalytical). For measuring, the intern program "omnian10 neu" was used which searches for all elements of the periodic table (PSE) in the sample and reports their concentration in the percentage of normalization to 100%.

The ICP-MS and LA-ICP-MS measurements were conducted by Lisa Laa from the research group for surface and trace analysis at TU Wien and Claudia Steinbach from the electrochemistry group.

ICP-MS measurements allow a multi-element analysis of liquid samples with a low detection limit and easy sample preparation. The sample solutions are transferred into an aerosol within the sample inlet system. This aerosol is then introduced into plasma where solvent evaporation, sample atomization and ionization take place. The generated ions enter the mass spectrometer over an interface system where they are further analyzed. The MS signals can be matched with concentration values over an external calibration. [57]

Solid samples can be measured directly with the LA-ICP-MS technique. Herein, the samples are put into an ablation chamber under an inert gas atmosphere, where they are exposed to short pulses of a high-irradiance laser, and small craters occur on the sample surface. The vaporization process generates an aerosol, which is then transferred to the ICP-MS system over an inert gas flow. The unique characteristics of this method include the possibility of depth profiling and surface mapping, while the laser beam is scanned over the sample surface. In addition, no sample preparation is needed which allows for a high throughput analysis. [58]

The LA-ICP-MS system used a TwoVol2 laser ablation chamber (Elemental Scientific) with an excimer laser with a wavelength of 193 nm(Elemental Scientific). Argon, fluorine and helium acted as buffer gases. The targets were directly introduced into the ablation chamber, several line scans were performed to obtain a better statistic. An external calibration with solid-state pellets was used to quantify the Li, La and Ti content. The mass and molar compositions of the samples could then be calculated.

The ICP-MS setup consisted of an iCAP Q ICP-MS system (ThermoFisher Scientific) with a quadrupole mass analyzer. The surface of the target was ground and the resulting powder was dissolved in concentrated HCl (37 % HCl, VWR Chemicals) through heating in a water bath for several hours. A liquid multi-component standard was prepared with a dilute 3 % HNO_3 (65.0 - 67.0 % HNO_3, Sigma-Aldrich) solution for the calibration curve.

Additionally, impedance spectra of an LLTO target were recorded, using a VMP-300 potentiostat (BioLogic). The back and front of a sintered target were coated with a 100 nm layer of platinum. The cylinder coat was ground afterwards to prevent short-circuit measurements. The target was placed in a measuring cell, where it was fixed and contacted with metal screws. The measuring cell itself was put into a metal box due to electrical shielding problems. The measurements were conducted in a frequency range from 1 MHz to 0.1 Hz, with a sinus amplitude of 10 mV and in an E-range from -5 V to 5 V.

3.1.2 Li_3PO_4 targets

The starting material for the LIPON targets was lithium phosphate powder (Li_3PO_4, Sigma-Aldrich, CAS Nr. 10377-52-3). The powder was very flaky, therefore a pre-compressing step was necessary before the actual pellet-pressing process. To do so, the powder was carefully compressed in a mortar and was then transferred into the press die. The manufacturing was carried out under the same conditions as for the LLTO targets. Nevertheless, there were two differences. Firstly, no press wax was added. Secondly, there were major problems with the pellet pressing step because the press stamp got stuck several times due to the fine powder grain. Therefore, the pellet was often pressed twice.

In Table 3.2 the produced targets and their manufacturing conditions are summarised.

Table 3.2: Manufacturing conditions of Li_3PO_4 targets

sample	time (h)	temperature (°C)	heating ramp (°Cmin^{-1})	pressure (bar)	appearance
26.04	12	600	-	260	porous, flat
29.04	4	750	-	347	small pores, little cracks on edges
04.05	12	900	-	347	flat, little pores
12.05	6	800	-	347	flat and compact
20.05, profile	4	750	200-400-750	347	flat, little pores
31.05, ramp	4	750	2	347	very porous
02.06	4	750	500-750	260	flat, little pores

The sintering of target 20.05 was performed with two 20 min temperature holding steps at 200 °C and 400 °C with an applied heating ramp of 6 °Cmin^{-1}. Afterwards, the target was heated to the final sintering temperature of 750 °C.
Target 02.06 was heated with a 5 °Cmin^{-1} ramp to a temperature of 500 °C where the temperature was held for 20 min. Then the temperature was raised to the sintering temperature with a 10 °Cmin^{-1} ramp.

3.2 Thin film sputtering

It was originally planned to sputter solid LLTO and LIPON thin films with the as-produced targets and to further test their chemical and electrochemical properties. It is reported in the literature that a very low base pressure is necessary for LIPON sputtering. The reachable base pressure of the sputtering machine was, however, in the region of 10^{-4} mbar, which is too high. It was therefore decided to concentrate on LLTO sputtering.

The substrates for the thin films were 10 x 10 mm silicon (Infineon) and sapphire (sapphire (0001)K $< 0.1°$, one side polished, CrysTec) single crystals. The silicon crystals were used as a substrate for XRF and analytical measurements, whereas the sapphire single crystals were used as substrates for electrochemical characterization measurements.

The following paragraph describes the procedure for LLTO thin film sputtering. A sputter gun for targets with a diameter of 2.54 cm was used (Zhengzhou CY Scientific Instrument Co., Ltd.). A temperature calibration with a pyrometer (Heitronics KT 1999) was conducted to enable hot sputtering. Herein, the temperature shift between the thermocouple and the substrate temperature, measured with the pyrometer, was evaluated.
Before every sputtering process, the sputter target was dismantled from the sputter gun and ground with abrasive paper to remove residues from previous sputtering experiments. Additionally, the substrate was cleaned with compressed nitrogen to remove any particles from the surface and was placed on the sample holder inside the chamber. The cooling water and the vacuum pumps got switched on. The chamber was evacuated via the backing pump and the turbomolecular pump was switched on as the pressure reached 1 mbar. The chamber was evacuated to the low 10^{-4} mbar region, then the gases were led into the chamber. For LLTO sputtering, argon (Ar) and oxygen (O_2) were used in a mixing ratio of 7/8 Ar (40 sccm) and 1/8 O_2 (6 sccm). The gas flow was controlled via mass flow controllers (MFC, tylan FC-260) and was set via a flow controller (Aera ROD-4).
Heating of the samples was required to obtain crystalline films. The voltage of the heating device was controlled with a power supply unit (Voltcraft HPS-13015). A heating ramp of $45\,°\mathrm{Cmin}^{-1}$ was applied until the temperature was reached. After about 10 min the sputtering process was started at the desired temperature. The plasma power was set with a plasma generator (plasma generator Kurt J. Lesker RX01/LX01 series radio frequency power supply). A pre-sputtering of the target was performed for 10 min where a stable plasma atmosphere should be generated. Herein, the target was shielded with a shutter, a rotating stainless steel sheet.
A cooling ramp of $30\,°\mathrm{Cmin}^{-1}$ was applied for hot sputtered samples after the sputtering process.

In the course of the experiments, the sputtering parameters were varied, including gas pressure, sputtering time, plasma power, target to substrate distance and temperature.

Annotation: In section 3.3 the optimization work of the sputtering machine is described. The smaller recipient, which enables hot sputtering, was mounted at the relative end of the practical work. Heating of the sputtered samples was, until then, performed with post-annealing steps. The samples were placed in a corundum crucible in a furnace, where a heating ramp of 2 °Cmin^{-1} was applied.

The characterization methods of the sputtered thin films can be distinguished into four main categories.

3.2.1 Structural characterization techniques

A major part of the structural characterization consisted of XRD measurements. Two measurement modes were applied for the analysis of film samples, the standard method using an X'Pert MPDII device (Philips) and the grazing incidence (GID) technique using an Empyrean material diffractometer (PANalytical) with Cu-K$_\alpha$ radiation (45 kV, 40 mA). The latter offers the possibility to individualize the measurement setup, allowing GID measurements. Herein, a small angle of incidence of the X-ray beam is utilized. This has the consequence that the measurement is very surface sensitive due to the small penetration depth. Thin films can be measured effectively as a strong background signal from the substrate materials is mostly prevented. [59] Nevertheless, overlapping of sample and substrate reflexes can still occur.

The GID analysis was conducted with a relatively large incidence angle of 5°. The GID setup included the following items: Chi-Phi-Z (reflection) 240 nm sample stage, incident beam optics with a 0.04 soller slit, 4/6 mask and $\frac{1}{2}/\frac{1}{4}$ divergence slit, diffracted beam optics with a PreFix parallel plate collimator connected to a scintillation detector. There was the option to use an automatic reflection spinner sample stage instead of the manual Chi-Phi-Z stage. Nevertheless, the manual stage was preferentially used. The position of every sample was calibrated before every measurement, which included the setting of calibration offsets through 2θ, Z and Ω-scans. Therefore, a precise measurement environment was generated for every sample.

In-situ post-annealing XRD measurements were carried out on an X'Pert MPDIII (PANalytical) device in Bragg-Brentano geometry with Cu-K$_\alpha$ radiation (45 kV, 40 mA). Herein, a sample was heated along a temperature program, and at every temperature step, a diffractogram was recorded. From room temperature (25 °C) onwards, heating was done in 100 °C increments to the end temperature of 1200 °C. Afterwards, the sample was cooled to 50 °C and another diffractogram was measured. The reaction medium consisted of compressed air. With this method, the crystallization process of amorphous samples can be observed.

3.2.2 Chemical characterization techniques

For the chemical characterization, XRF, LA-ICP-MS and ICP-MS measurements were carried out under the same procedure as for the target measurements.

The thin films and the LLTO powder got dissolved in concentrated HCl through heating in a water bath, where a minimum time of 2 h was necessary to dissolve the powder itself. A dilution series of the thin film samples with a 3 % HNO_3 was prepared. Liquid multi-component standards were used for the calibration line. No mass composition could be calculated because the masses of the dissolved films were unknown. Instead, a molar composition was specified.

3.2.3 Surface characterization techniques

Atomic force microscopy (AFM), scanning electron microscopy (SEM) and profilometer film thickness measurements were performed to get a better understanding of the surface structure referring to crystallinity, pinhole density and overall roughness.

The AFM measurements were conducted in tapping mode with a NanoScope V Multimode setup (Veeco Instruments) where an area of 1 x 1 μm^2 was scanned.

The SEM measurements were carried out on a Quanta 200 FEG with a Schottky Emitter (FEI) with varying operation voltages. Beforehand, the samples were coated with a 5 nm Au/Pd thin film to prevent charge effects as the samples are insulators.

The profilometer scans were executed with a DekTak XT (Bruker) with the analysis software Vision64. Two types of measurement modes were carried out. Firstly, it was tried to measure the thickness of the sputtered films. To do so, the corners of the substrates were brushed with a zirconium dioxide paste (ZrO_2, 99.7 %, Thermo scientific, in terpineol, Aldrich Chemistry) before sputtering. After film deposition, the paste was removed with cotton swabs and ethanol. This resulted in blank corners where the thickness difference to the sputtered films could be measured. Secondly, line scans over a greater part of the surface were conducted to obtain information about the overall topology.

3.2.4 Electrochemical characterization technique

Impedance spectroscopy was conducted to characterize the samples in an electrochemical way. For sample preparation, the back of a sapphire substrate was coated with a 100 nm platinum film (Pt) and the front with a 5 nm titanium and a 100 nm platinum (Ti/Pt) layer. The titanium acted as an adhesion layer for the platinum film. The sputtering was conducted on a BAL-TEC MED 020 Coating System (Pt target from Ögussa, Ti target from Micro to Nano).

Afterwards, the LLTO film could be sputtered on the substrate. Microelectrodes were deposited on top of the film with the use of a shadow mask. The microelectrodes had a thickness of 100 nm and a diameter of approx. 550 μm. This design, consisting of Pt-sapphire-Ti/Pt-LLTO-Pt layers, is called sandwich structure. The LLTO electrolyte is centred between electrically conductive layers which allows cross-plane impedance measurements. The sample is contacted from both sides, where the working electrode contacts the microelectrode on top of the film. Herein, a characterization of the electrolyte itself is possible. In Figure 3.1 a schematic drawing of the sandwich structure is shown.

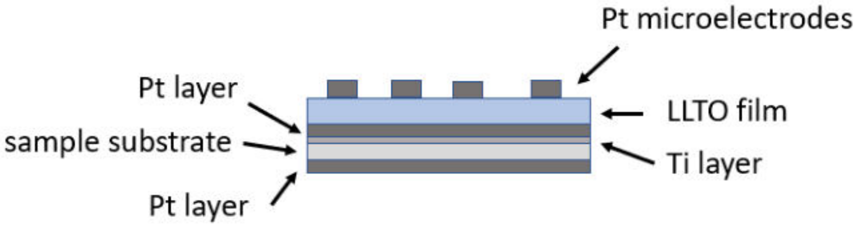

Figure 3.1: Schematic drawing of the sandwich structure; the LLTO film (blue) is surrounded by conducting platinum layers (dark grey), the Ti film (light grey) acts as an adhesion layer for the substrate (white)

The samples were introduced into a measuring station with an optical FS70Z-S microscope (Mitutoyo), a camera and micromanipulators, where the microelectrodes could be contacted more easily. The used electrodes consisted of thin platinum needles. The measurements were conducted using an Alpha-A High Performance Frequency Analyzer (Novocontrol). A frequency range of 10^6 Hz to 1 Hz respectively 0.1 Hz was covered, where a resolution of 10 points per decade and an output voltage of 0.02 V were used. The measurements took place at room temperature in ambient air.

In a series of measurements, impedance spectra were recorded at different temperatures, namely at 40 °C, 60 °C, 80 °C, 100 °C, 120 °C and 400 °C. The temperature of the heater, Linkam TS 1000 (Linkam Scientific Instruments), was monitored with a thermocouple.

3.3 Optimization of the sputtering machine

A sputtering machine with an RF magnetron plasma generator was used for sputtering thin film samples. The machine was constantly improved throughout the work on this thesis as several modifications were carried out. In the following section, an overview of the construction work is given.

The initial setup consisted of the following items:

- backing pump
- turbomolecular pump
- glass recipient with plexiglass for splinter shielding
- chamber with a moveable sample stage on a rotary shaft
- sample holder on the sample stage with a mounted light bulb for heating; the sample holder itself was formed of curved water cooling tubes
- external water cooling system for the sample stage which was switched in series with the water cooling for the sputter gun
- sputter gun for 5.08 cm diameter targets in the chamber lid
- shutter for the sputter gun
- RF magnetron generator
- thermocouple for temperature monitoring
- two pressure cells

In Figure 3.2 and 3.3, two pictures of the adapted sputtering machine setup are shown.

The major drawback of the sputtering machine was the reachable base pressure. In the first setup, a base pressure in the high 10^{-4} mbar region could be achieved. This value was too high for the following sputtering experiments. Hereby, a base pressure in the region of 10^{-6} mbar would have been the goal. However, the construction setup limited the possibilities. A base pressure reduction to the low 10^{-5} mbar was therefore aimed at. Initially, stainless steel water tubes were used inside the chamber for the water cooling system. However, it was found that they were leaking, which lowered the reachable base pressure. In addition, they were of very rigid structure, making the rotation of the sample stage difficult. The whole water cooling system got changed. A pipe penetration setup was mounted at the bottom of the chamber. Copper water pipes, two voltage cables for the electric heater and a thermocouple cable were led through this system. The water tubes were directly connected to the sample holder and the electric cables were isolated with shrink tubes and ceramic sleeves to avoid short-circuits.
The base pressure could be lowered to the high 10^{-5} mbar region in the new setup.

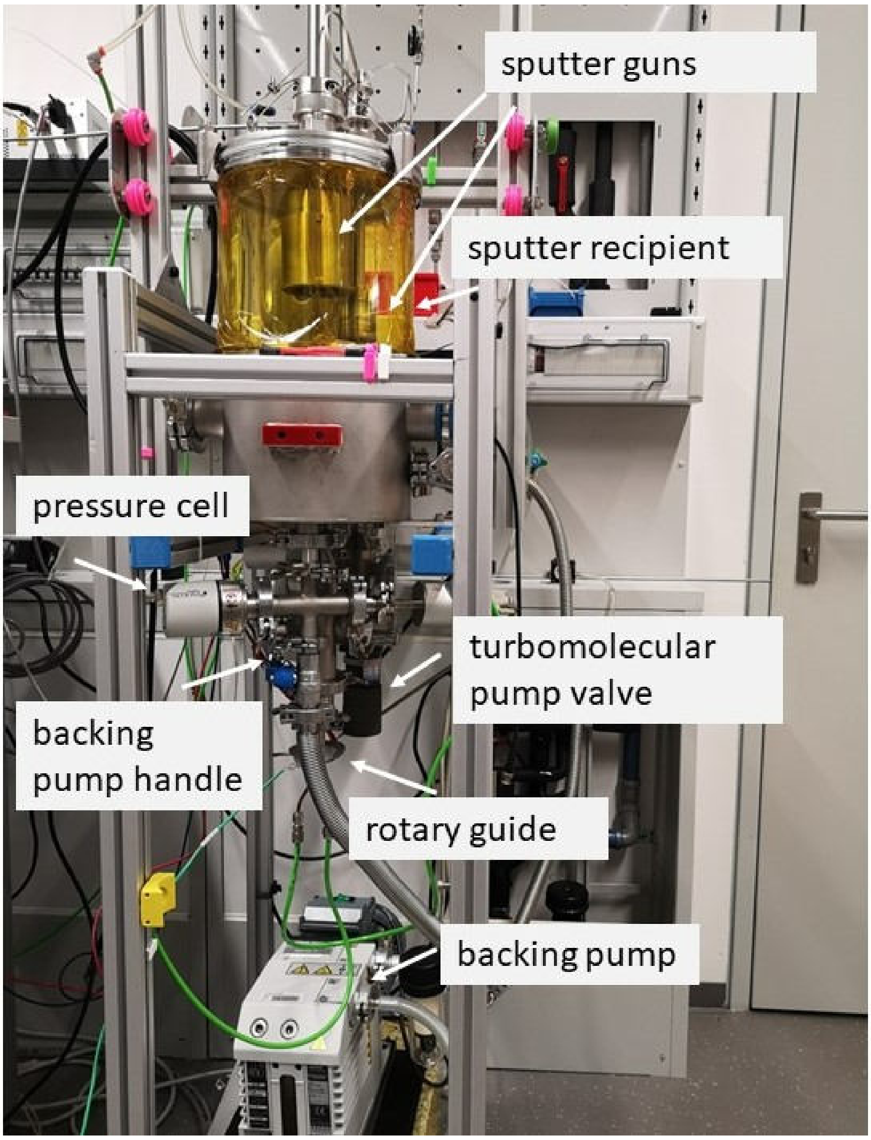

Figure 3.2: Sputtering machine: an overview of the machine with essential components

A sputter gun for targets with a diameter of 2.54 cm was additionally installed to the sputter gun for 5.08 cm targets. The sputter guns were mounted in the lid of the sputtering machine.

The heating of the substrates was performed with a 24 V light bulb, which was placed in the sample holder directly under the sample substrate. The temperature was controlled with a power supply unit and was measured via a thermocouple of type K, mounted inside the sample holder near the light bulb.

The vertical distance between the target and sample is crucial in sputtering experiments. The shaft of the small sputter gun was considerably shorter than that of the large gun, leading to an increased distance between the target and the sample. It was therefore not

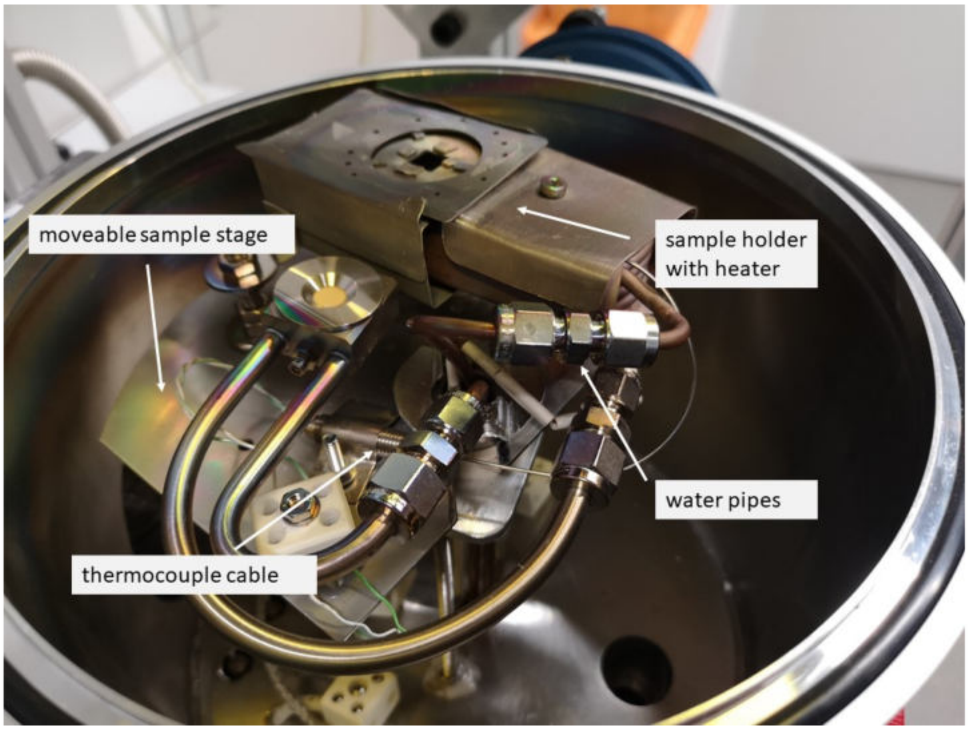

Figure 3.3: Sputtering machine: inside look in the chamber with sample stage and heater

possible to perform hot sputtering with the small gun as no film growth could be experienced at this distance. A smaller glass recipient was introduced in the last construction step. Adhesive tape on the outside of the recipient was used as splinter shielding.

Chapter 4

Results and Discussion

4.1 LLTO target characterization

The following paragraph covers the general target manufacturing process.
In the process of powder pressing, it could happen that the pellet broke or showed cracks. It was therefore necessary to grind the pellet and press it again. This cycle should not be repeated more than three times as the ground powder would become more crumbly with every step, which resulted in an even worse pellet structure. Two factors affected the probability of a crack formation, the thickness of the produced pellet and the applied pressure. The thickness should be in a range of 0.3 cm as it turned out that a thicker pellet is more prone to cracks during pressing and the following sintering step. Furthermore, a thick pellet was rather curved than flat after sintering.
The used working pressure was usually 260 bar. A higher pressure should be avoided because otherwise more cracks will occur.

The targets were sintered with different sintering programs where the sintering temperature, the heating/cooling rate and the sintering time were modified. The goal was to find a program, which resulted in a flat and dense pellet which did not show signs of phase transformations or impurities. The main characterization method for the target analysis were XRD measurements.

4.1.1 Structural characterization of LLTO targets

In Table 4.1 the produced LLTO targets are assigned to an XRD reference file through the use of the evaluation software HighScore, and the space group is given as well. Additionally, a Rietveld refinement was carried out where the cell parameters were obtained. Hereby, the volume per formula unit (volume p.f.u) is calculated. The associated diffractograms are displayed in Figure 4.1, where Figure 4.2 shows an enlargement of a major reflex at 32°. Hereby, the initial LLTO powder was measured as well to account for differences in the pellets' diffractograms, respectively to examine the phase shifts of the reflex positions.

Table 4.1: XRD analysis: an overview of LLTO targets with the parameters of the Rietveld refinement

sample	reference file	a (Å)	b (Å)	c (Å)	density (gcm^{-3})	volume p.f.u ($Å^3$)
ref., $Li_{0.33}La_{0.56}TiO_3$	04-017-8119, Cmmm65	7.7340	7.7300	7.7550	-	57.95
ref., $Li_{0.18}La_{0.61}TiO_3$	04-014-3535, Cmmm65	7.7660	7.7680	7.8250	-	59.01
ref., $Li_{0.21}La_{0.60}TiO_3$	04-024-7880, P4/mmm123	3.8714	3.8714	7.7789	-	58.29
ref., $Li_{0.24}La_{0.59}TiO_3$	04-020-7088, P4/mmm123	3.8700	3.8700	7.7800	-	58.26
LLTO powder	04-020-7088	3.8661	3.8661	7.7761	5.03	58.11
15.04	-	-	-	-	3.44	-
24.05	04-017-8119	7.7369	7.7264	7.7639	3.72	58.01
07.06	04-014-3535	7.7254	7.7356	7.7590	-	57.96
18.07	04-024-7880	3.8656	3.8656	7.7657	4.47	58.02
04.08	04-017-8119	7.7405	7.7276	7.7626	-	58.04
05.09	04-017-8119	7.7397	7.7269	7.7592	3.83	58.00
08.09	04-017-8119	7.7393	7.7265	7.7633	3.89	58.03

It can be seen from Figure 4.1 that the sintered LLTO targets are phase pure and exhibit no impurities as their reflexes match well with those of the LLTO powder. There is only a shift in the exact reflex position. Consequently, the targets can be identified as LLTO.

The first produced target, sample 15.04 with a sintering temperature of 1050 °C and a sintering time of 48 h, resulted in a quite porous pellet which could not be assigned to a reference file. The following targets, which were sintered at 1100 °C for 8 h, resulted in more compact pellets which were assignable with the XRD database. An additional improvement of the structure was experienced when a heating ramp of 10 °Cmin^{-1} was applied.

The results of the phase shift analysis are presented in Table 4.2. Herein, the most intense reflexes of the LLTO powder diffractogram are identified and the deviation to the reflex position of the single targets is calculated in per cent.

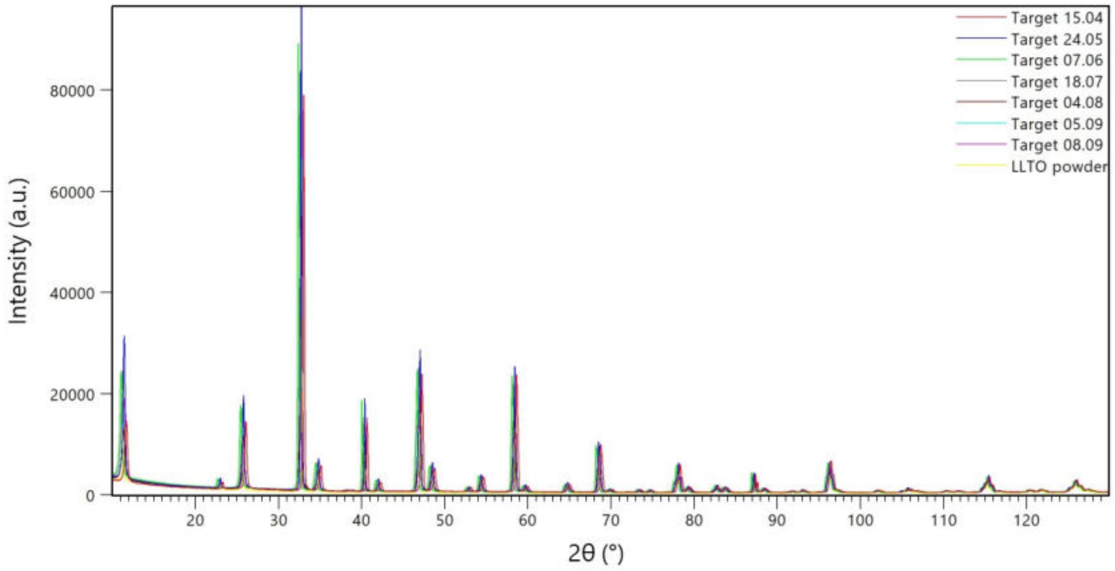

Figure 4.1: $\Theta - 2\Theta$ diffraction pattern: comparison of LLTO targets and LLTO powder

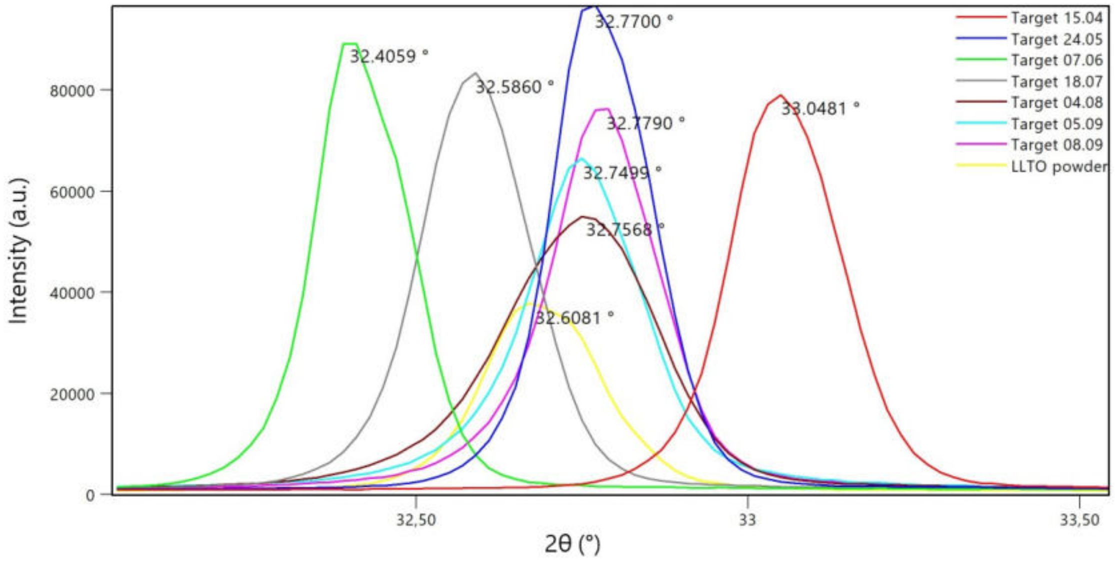

Figure 4.2: $\Theta - 2\Theta$ diffraction pattern: zoom at 32° to observe the sequence of the LLTO targets and the LLTO powder; colour code: target 15.04 (red), 24.05 (dark blue), 07.06 (green), 18.07 (grey), 04.08 (brown), 05.09 (light blue), 08.09 (pink), LLTO powder (yellow)

Target 15.04 exhibits the largest deviation in the reflex positions to the LLTO powder. This is of no surprise as this target was not assignable with the XRD database and resulted in a porous product. Interestingly, targets 24.05 and 07.06 differ from one another strongly, although they were made under the same conditions. This is also the case for

Table 4.2: Analysis of the shift in the reflex positions of the LLTO powder reflexes to the reflexes of the single targets

LLTO powder reflex position (°2Θ)	15.04	24.05	07.06	18.07	04.08	05.09	08.09
	(deviation in percent to LLTO powder)						
11.37	2.74	0.70	-2.64	-0.97	0.70	0.26	0.35
25.72	1.38	0.35	-1.05	-0.43	0.19	0.31	0.47
32.64	1.15	0.31	-0.80	-0.21	0.40	0.31	0.40
40.3	0.84	0.20	-0.67	-0.25	0.30	0.17	0.25
46.97	0.63	0.15	-0.60	-0.23	-0.02	0.09	0.13
58.36	0.53	0.14	-0.43	-0.15	0.05	0.10	0.12

target 18.07 and the series from 04.08 to 08.09. They appear on each side of the LLTO powder reflex in Figure 4.2. The calculated values for the volume per formula unit do not differ significantly within the target series. However, their values are smaller compared to the LLTO powder which accounts for a reduced unit cell. Nevertheless, it can be concluded that the target series 04.08 to 08.09 does match well with the LLTO powder diffractogram.

The structure of the LLTO powder is assigned to a tetragonal phase, whereas the targets crystallize in an orthorhombic phase. This change in the crystal structure indicates the loss of lithium during sintering as already discussed in the theoretical part. In literature, the orthorhombic lattice is reported for a lithium content in the range of $0.12 < x < 0.2$. [60] Interestingly, target 18.07 is assigned to the tetragonal phase, but the following targets, which were made under the same conditions, belong to the orthorhombic phase.

To evaluate the porosity of the sintered targets their density was calculated using the mass and geometric dimensions, where the form of a perfect cylinder was assumed. The density of the targets was then compared to the density of an LLTO unit cell, calculated from the molar mass of the elements and the unit cell parameters of the LLTO powder Rietveld refinement. The pellets' densities increased from $3.44\,\mathrm{g\,cm^{-3}}$ of target 15.04, relative density of 0.68 to the LLTO powder, to $4.47\,\mathrm{g\,cm^{-3}}$ of target 18.07, relative density of 0.88. This behaviour confirms the trend that high-temperature sintering with a shorter time results in denser pellets.
Interestingly, the density of target 18.07 marks the highest density among all samples, the following targets do have smaller densities in the range of $3.83\,\mathrm{g\,cm^{-3}}$, the relative density of 0.76, although they were all made under the same conditions.

4.1.2 Chemical characterization of LLTO targets

For an additional characterization, Raman measurements were conducted where one target (7.6) and an LLTO sheet ($Li_{0.29}La_{0.57}TiO_3$, TOHO TITANIUM CO., LTD.) were measured. Figure 4.3 shows an overview of the recorded spectra with a mode assignment according to literature data. [61]

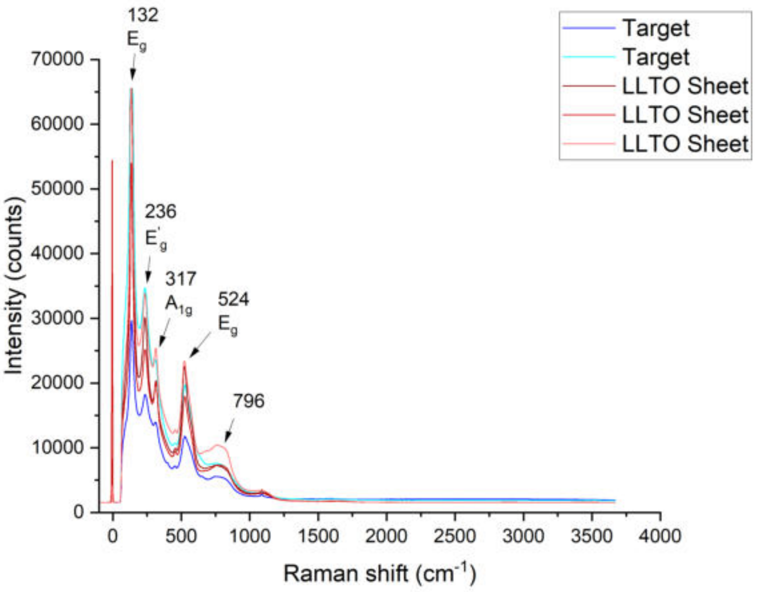

Figure 4.3: Raman spectra of LLTO sheet and target 07.06 with the assignment of the bands

The target matches nearly perfectly with the LLTO sheet which is a further indication for the target identification as LLTO.

Furthermore, XRF measurements were conducted which allow a quick analysis of the elemental composition. It has to be noted that these results are interpreted qualitatively. On the one hand, oxygen, which is a major component of LLTO, is quite difficult to measure and may distort the measurement. On the other hand, no solid standards were produced for a calibration curve. The manufacturing of homogeneous standards would have gone beyond the scope. Furthermore, lithium can not be analyzed because of the extinction rules for electronic transitions.

A pellet for the LLTO powder measurement was prepared through of the bulk powder with 10% press wax and a following pressing step.

In Table 4.3 the results of the elemental composition of the measurements are shown. In addition, the element ratios are calculated for the better identification of sample trends as for the absolute numbers.

Table 4.3: Measurement results of the XRF LLTO target analysis with elemental ratios

sample	La (%)	Ti (%)	O (%)	La/Ti	La/O	Ti/O
15.04	38.812	26.901	34.287	1.443	1.132	0.785
07.06	38.514	27.142	34.344	1.419	1.121	0.790
18.07	37.009	26.801	35.302	1.381	1.048	0.759
04.08	53.635	28.086	31.208	1.910	1.719	0.900
LLTO powder	45.419	30.898	23.641	1.470	1.921	1.307
LLTO sheet	34.771	26.288	38.158	1.323	0.911	0.689

The XRF measurements confirmed the presence of lanthanum, oxygen and titanium, where sometimes minor impurities were present. Two statements can be made from the result table in Table 4.3. Firstly, the targets match well in their composition, except for target 04.08, where no explanation can be found. Secondly, the elemental concentration of the targets comes close to that of the LLTO sheet but deviates from the LLTO powder. Herein, the press wax in the LLTO powder pellet, which was not sintered, could distort the results.

ICP-MS and LA-ICP-MS measurements were performed for a more detailed chemical analysis.

Two ICP-MS analyses were carried out where target 04.08 was measured both times. However, different results were obtained. The first time, only the lithium to lanthanum ratio (Li/La) could be calculated, resulting in a value of 0.83. In the second measurement, it was possible to determine the stoichiometry, which gave a molar composition of $Li_{0.33}La_{0.53}TiO_3$ and a Li/La ratio of 0.62.

A meaningful measurement requires that all elements get dissolved equally well. During sample preparation, however, it was found that the ground target powder did not dissolve well. In addition, it is reported that titanium gets easily deposited on the tube wall. The analytical result is depending on the extent to which the powder has dissolved and can therefore vary. It is thereby also possible that larger Li/La ratios are obtained for the target than for the LLTO powder (Li/La ratio of 0.51) and that the individual values for the target differ.

The LA-ICP-MS measurements were quite challenging. The produced pellets for the calibration curve were customized for the LLTO powder of the Li, La and Ti content. The matrix of the sintered targets differs from those of the pellets. Therefore, a matrix effect is present which directly affects the laser ablation and, as a result, the quantification of the elements. Furthermore, severe plasma issues occurred during the first measurement. In total, it was only possible to measure a single target, 18.07, where the molar composition can be specified to $Li_{0.43}La_{0.28}TiO_3$ and the weight composition to Li 2.81 wt%, La 38.31 wt%, Ti 47.94 wt%. Nevertheless, this result has to be treated with caution.

4.1.3 Electrochemical characterization of LLTO targets

Impedance spectroscopy was conducted where a target, which was sintered at 1050 °C for 24 h, was measured. The Nyquist plots of one measurement cycle are displayed in Figure 4.4, where the enlarged high-frequency region is shown in Figure 4.5.

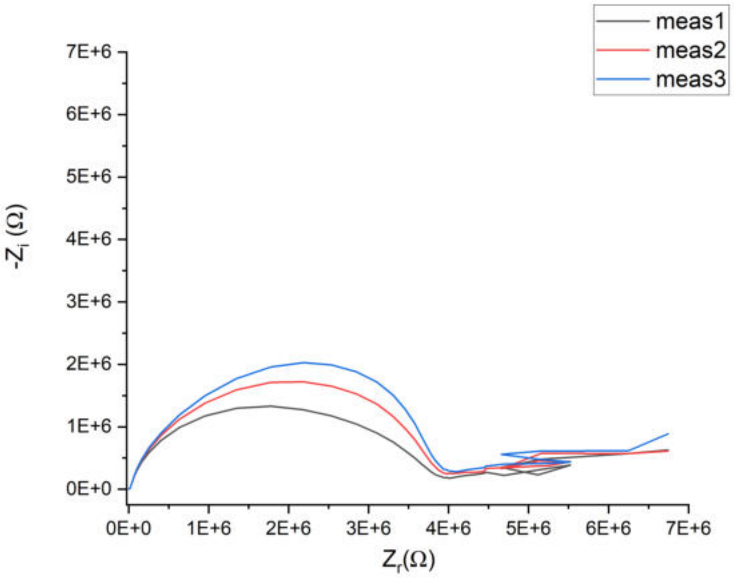

Figure 4.4: Nyquist plot from the impedance measurement of one LLTO target, three cycles were carried out

The zoom into the high-frequency region of the Nyquist plot displays a small semicircle with an oblique straight. This straight merges into the large semicircle which does not intercept the x-axis. These patterns of a small semicircle followed by a larger semicircle indicate the presence of a grain and grain boundary resistance. Furthermore, it can be seen from Figure 4.4 that the size of the semicircles increases with the progression of the measurement series. This behaviour can be attributed to the balance adjustment of the system. In the software EC-Lab, the impedance spectra were fitted with an equivalent circuit. The high-frequency semicircle was fitted with an R/Q+Q circuit (parallel circuit of resistor (R) and constant phase element (Q) with another constant phase element in series) where a part of the low-frequency semicircle is used for the serial attachment of the second constant phase element. The low-frequency semicircle was fitted with a single

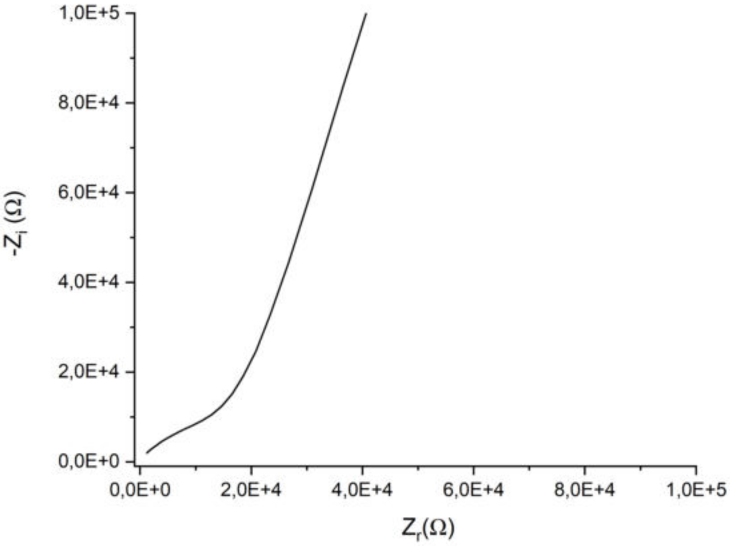

Figure 4.5: Zoom into the high-frequency region of the Nyquist plot from the first LLTO target measurement

R/Q circuit. The ionic conductivity and the capacitance could be calculated from the obtained parameters of the equivalent circuit fit. The measured target was 0.4 cm thick and had a diameter of 2.24 cm. The theoretical capacitance is calculated according to Equation 2.11, with $\epsilon_\mathrm{r} = 150$ for LLTO [62], to $4.76 \cdot 10^{-10}$ F.

For the smaller, high-frequency semicircle the mean of the ionic conductivity is calculated to $1.59 \cdot 10^{-6}$ Scm^{-1} and of the capacitance to $2.03 \cdot 10^{-10}$ F. The ionic conductivity for the large arc results to $4.85 \cdot 10^{-9}$ Scm^{-1}, with a capacitance of $4.05 \cdot 10^{-9}$ F. Due to the low capacitance, the high-frequency semicircle is attributed to the grain conductivity and the low-frequency semicircle to the grain boundary conductivity. However, the ionic conductivity for the bulk is much smaller in comparison to literature values. One explanation would be that the actual bulk conductivity is hidden in the offset of the Nyquist plot. Hereby, the previously assumed bulk semicircle would then be assigned to the grain boundary resistance and the large, low-frequency semicircle to an electrode feature. However, also lithium loss during sintering may have occurred which lowers the bulk conductivity and permittivity.

In conclusion, the produced targets can be identified as LLTO, where no phase transformation or impurities were observed. Sintering at higher temperatures and with a heating ramp of 10 °Cmin^{-1} results in optically dense targets. In addition, the diffractograms are also more similar to the one of the LLTO powder.

4.2 Li_3PO_4 target characterization

The structural analysis of the Li_3PO_4 targets was conducted with XRD measurements. In Table 4.4, the assignment of the targets to reference files and the results from the Rietveld refinement are displayed. In Figure 4.6 an overview of the targets' diffractograms is depicted. A zoom is shown in 4.7 to get a better insight into the sequence of the samples.

Table 4.4: XRD analysis: overview of Li_3PO_4 targets with the parameters of the Rietveld refinement

sample	reference file	a (Å)	b (Å)	c (Å)	density (gcm^{-3})	volume p.f.u ($Å^3$)
reference file	04-006-8566, Pmnb62	6.1113	10.4612	4.9208	-	78.649
reference file	04-007-2815, Pnma62	10.4900	6.1200	4.9266	-	79.070
reference file	04-015-2197, Pnma62	10.5800	6.1700	4.9900	-	81.435
reference file	04-008-2093, Pmnb62	6.1200	10.5300	4.9300	-	79.427
Li_3PO_4 powder	04-006-8566	10.4897	6.1200	4.9079	-	78.768
26.04	04-006-8566	10.4734	6.1154	4.9235	2.01	78.836
29.04	04-006-8566	10.4725	6.1162	4.9233	1.93	78.836
04.05	04-006-8566	10.4681	6.1163	4.9239	1.99	78.816
12.05	04-015-2197	10.4727	6.1158	4.9233	1.97	78.833
20.05	04-008-2093	10.4728	6.1162	4.9234	2.01	78.842
31.05	04-007-2815	10.4727	6.1163	4.9235	1.84	78.842
02.06	04-006-8566	10.4721	6.1155	4.9229	1.97	78.820

The targets sintered at a temperature of 750 °C, namely 29.04, 20.05, 31.05 and 02.06, are grouped in the middle of the zoomed diffractogram. Target 12.05, sintered at 800 °C, appears at the smallest angles and target 04.05, sintered at 900 °C, at the largest angles.

It is reported that Li_3PO_4 crystallizes in the β-phase at room temperature, where an irreversible transformation to the γ-phase takes place at approx. 450 °C. [63] Therefore, it was assumed that the starting powder would be present in the β-phase. However, through the Rietveld refinement, it turned out that the powder itself, and all the targets, crystallize in the γ-phase. It might be that through the manufacturing of the Li_3PO_4-powder the phase transformation already occurred.

To evaluate the shift in the reflex positions, the targets are compared to the reported 2Θ values from the XRD reference file 04-006-8566, where the most intense reflexes are

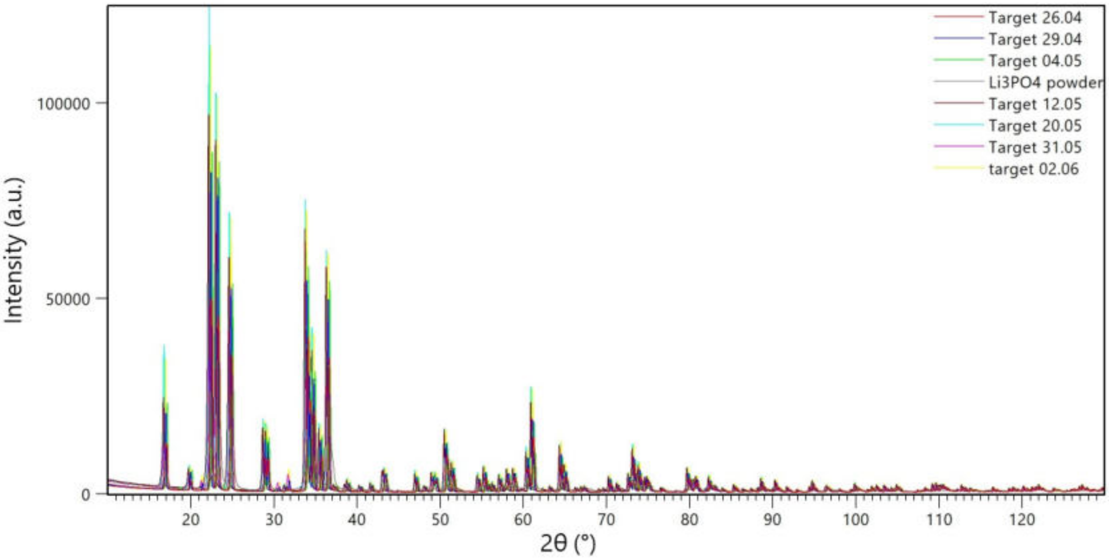

Figure 4.6: $\Theta - 2\Theta$ diffraction pattern: comparison of Li_3PO_4 targets and Li_3PO_4 powder

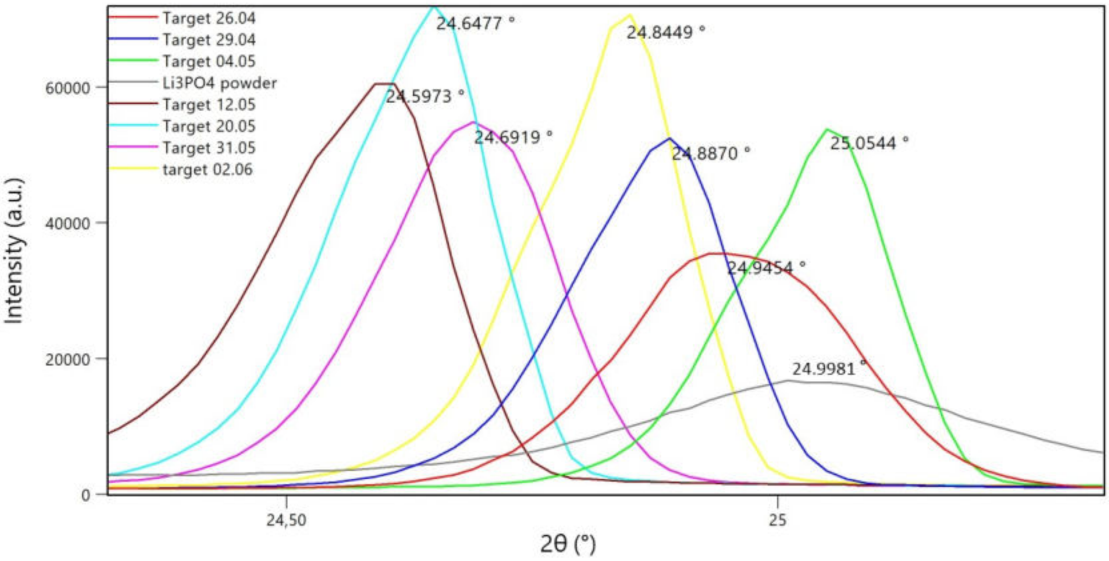

Figure 4.7: $\Theta - 2\Theta$ diffraction pattern: zoom at 24.5° to observe the sequence of the Li_3PO_4 targets and the Li_3PO_4 powder; colour code: target 26.04 (red), 29.04 (dark blue), 04.05 (green), Li_3PO_4 powder (grey), 12.05 (brown), 20.05 (light blue), 31.05 (pink), 02.06 (yellow)

analyzed. A reference file and not the measured starting powder itself is taken to secure the chemical identity of the γ-phase. The deviation of the reflex position is given in per cent, see Table 4.5.

Table 4.5: Analysis of the shift in the reflex positions of the Li_3PO_4 reference file to the single targets, the deviation is given in per cent

reflex position 04-006-8566	26.04	29.04	04.05	12.05	20.05	31.05	02.06
(°2Θ)	(deviation in percent to reference file)						
16.93	1.34	0.53	1.51	-2.17	-0.89	-0.71	0.24
22.35	0.84	0.36	1.06	-1.73	-0.72	-0.49	0.13
23.18	1.02	0.39	1.07	-1.58	-0.65	-0.43	0.17
29.20	0.65	0.27	0.75	-1.32	-0.59	-0.38	0.07
33.95	-	0.14	-	-1.17	-0.54	-0.39	0.03
34.26	-0.38	1.57	-0.28	0.23	0.73	1.05	1.45
36.49	0.19	0.16	0.58	-1.05	-0.47	-0.36	0.06
61.15	0.03	-0.02	0.24	-0.68	-0.36	-0.30	-0.36

The largest deviation in the reflex position to the reference file marks target 12.05, which was sintered at 800 °C. Target 02.06, which was sintered at 750 °C with a holding step at 500 °C, agrees best with the reference file. Generally, the targets with a sintering temperature of 750 °C exhibit a smaller deviation to the reference file than the ones which were sintered at other temperatures.

The density of the Li_3PO_4 powder is calculated to $2.45\,\mathrm{g\,cm^{-3}}$. Overall, the densities of the targets do not deviate much and are mainly located in the region of $2\,\mathrm{g\,cm^{-3}}$, relative density of 0.81. However, the targets differ strongly in their optical appearance. Target 26.04 displays one of the highest densities although it is very porous. The optically densest appearance marks target 02.06, which was sintered with the temperature program 500-750. Target 31.05, sintered at 750 °C with an applied temperature ramp, was very porous, whereas the temperature profile target, 20.05, did result in a compact pellet. Additionally, all targets display a larger unit cell in comparison to the bulk powder and the reference file 04-006-8566.

In conclusion, the targets sintered at 750 °C show the smallest deviation in the reflex position to the chosen XRD reference file. Furthermore, these targets appear optically dense, except for target 31.05 which is quite porous.

4.3 Optimization of LLTO sputtering deposition

The thickness, uniformity and lithium content of the films depend on the sputtering parameters, such as vertical target to sample distance, pressure, plasma power and sputtering duration. For sputtering rate optimization, several films were deposited on large (ca. 8 x 6 $\mathrm{cm^2}$) Si wafers, and a LLTO target was used.

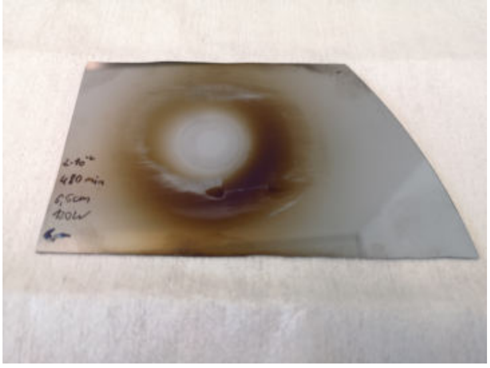

Figure 4.8: Image of sputtering test 1 on a silicon wafer, distance of 6.5 cm

Figure 4.9: Image of sputtering test 2 on a silicon wafer, distance of 5 cm, plasma power of 80 W

The sputtering of the optimization tests was carried out with the same procedure as for the thin film sputtering. Hereby, no sample heating was applied and the sputtering parameters were varied. The details of the conducted experiments are listed in Table 4.6, and the according pictures are shown in Figure 4.8 to 4.14. In Figure 4.11 and 4.12 the approximate positions of the sample substrates in the thin film sputtering, indicated by grey squares, are displayed.

Table 4.6: Sputtering deposition behaviour experiments

sample	pressure (mbar)	distance (cm)	plasma power (W)	sputtering time (min)
test 1	$2 \cdot 10^{-2}$	6.5	120	480
test 2	$8 \cdot 10^{-3}$	5	80	330
test 3	$1.5 \cdot 10^{-2}$	5	90	360
test 4	$1.5 \cdot 10^{-2}$	4.2	120	240
test 5	$9 \cdot 10^{-3}$	4	100	240
test 6	$1 \cdot 10^{-2}$	3	100	240
test 7	$1 \cdot 10^{-2}$	2	70	150

4.3.1 Sputtering deposition evaluation

In the following section, the sputtering deposition tests will be evaluated.

The most important parameter is the vertical target to substrate distance. The larger the distance, the blurrier the film becomes. Moreover, no deposition occurs in the middle of the substrate, directly below the centre of the sputter gun. This behaviour can be explained by the foundations of the RF magnetron sputtering technique. Herein, film

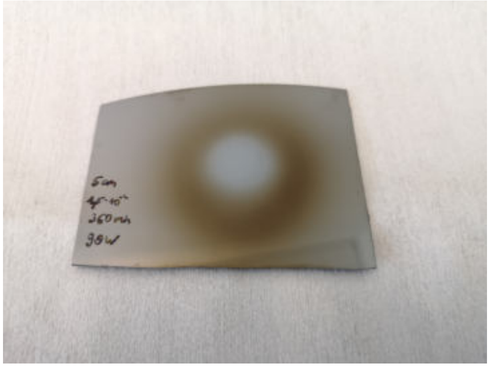

Figure 4.10: Image of sputtering test 3 on a silicon wafer, distance of 5 cm, plasma power of 90 W

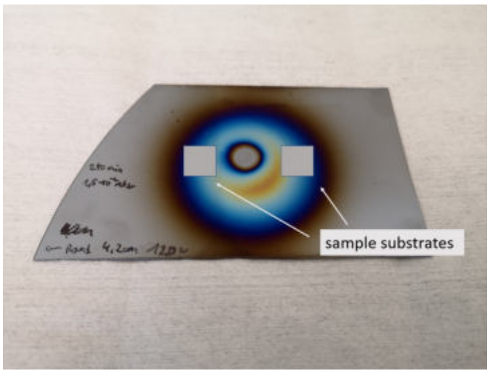

Figure 4.11: Image of sputtering test 4 on a silicon wafer, distance of 4.2 cm

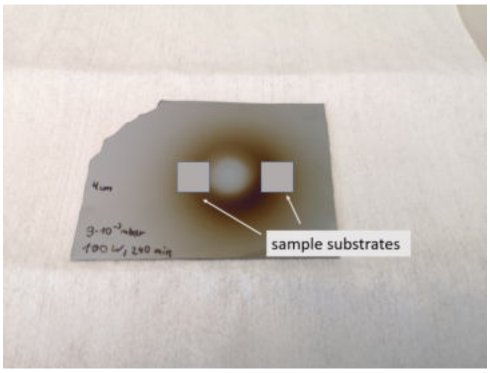

Figure 4.12: Image of sputtering test 5 on a silicon wafer, distance of 4 cm

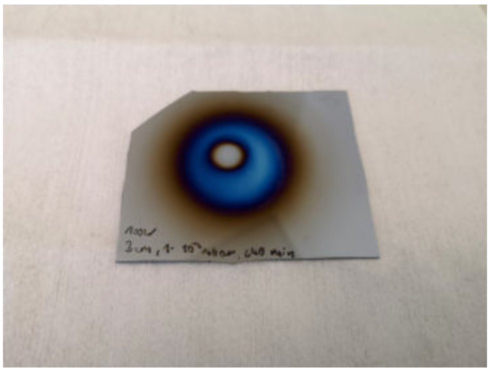

Figure 4.13: Image of sputtering test 6 on a silicon wafer, distance of 3 cm

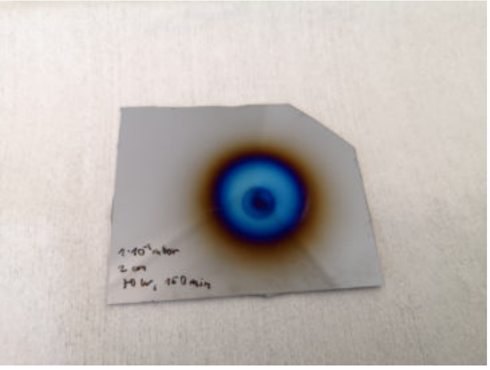

Figure 4.14: Image of sputtering test 7 on silicon wafer, distance of 2 cm

growth is experienced at the race track zone. The hole in the middle marks the region where no ion bombardment of the target takes place, therefore no film gets deposited and unintended back sputtering occurs. Sputtering test 7 marks the only experiment where the hole disappeared. It is assumed that due to the small distance the substrate lies within the plasma cone where sputtering effects act differently.

The formation of the hole gives further importance to the horizontal distance of the substrate to the centre of the sputter target. At positions directly underneath the centre, no sputter deposition will occur.

Another important parameter is plasma power. This parameter influences the layer thickness as can be seen in test 2 and test 3. The picture of test 3 appears to be sharper and darker in comparison to test 2. When the vertical distance is reduced, the plasma power needs to be decreased as well as otherwise the risk of back sputtering increases.

It is assumed that the gas pressure has no standalone effect on the sputtered films. Hereby, it is likely that the pressure influences the film through a combination of distance and power.

The sputtering time mainly influences the film thickness, which can be quantified at the film thickness measurement in subsubsection 4.4.3.1.

4.4 Analysis of LLTO thin films

In Table 4.7 an overview of the produced thin film LLTO samples is given. The manufacturing was carried out under the described procedure in the experimental section. The following labels are used in the table.

- Si: silicon substrate
- Ti/Pt: sapphire substrate with a 5 nm Ti and 100 nm Pt layer on the front and a 100 nm Pt layer on the back of the substrate
- TC: thermocouple temperature
- P: pyrometer temperature
- pa, ppa: post-annealed and double post-annealed samples

4.4.1 Structural characterization of LLTO thin films

XRD measurements were conducted for a characterization of the film structure of the sputtered samples. Herein, the standard and the GID measuring mode were used.

Until sample NR031, only background signals from the substrates were recorded, indicating an amorphous film structure. Hot sputtering has to be applied to generate crystalline films. Surprisingly, even the post-annealed samples NR021 and NR025 did not show any

Table 4.7: sputtered LLTO thin film sputtering parameters

sample	substrate	pressure ($\cdot 10^{-3}$ mbar)	distance (cm)	plasma power (W)	time (min)	heater	thickness (nm)
NR001	Si	10	4.2	120	300	pa 100°C, 2 h	123
NR002	Si	10	4.2	120	300	no heating	165
NR003	Si	30	4.2	120	300	pa 200 °C, 2 h	168
NR004	Ti/Pt	30	4.2	120	300	pa 200 °C, 2 h	-
NR005	Si	7	4.2	120	300	pa 300 °C, 2 h	77/141
NR006	Ti/Pt	7	4.2	120	300	no heating	-
NR007	Si	6	4.2	100	300	no heating	92/143
NR008	Ti/Pt	6	4.2	100	300	no heating	-
NR009	Si	9.5	6.5	120	350	no heating	45
NR010	Ti/Pt	9.5	6.5	120	350	no heating	-
NR011	Si	9.5	6.5	120	350	TC 200 °C	40
NR012	Ti/Pt	9.5	6.5	120	350	TC 200 °C, pa 400 °C, 2 h	-
NR013	Si	20	6.5	120	105	TC 200 °C	-
NR014	Ti/Pt	20	6.5	120	105	TC 200 °C, pa 500 °C, 2 h	-
NR015	Si	20	6.5	140	500	no heating	-
NR016	Ti/Pt	20	6.5	140	500	no heating	-
NR017	Si	9	4.2	120	300	no heating	-
NR018	Ti/Pt	9	4.2	120	300	no heating	-
NR019	Si	10	4	120	300	no heating	-
NR020	Ti/Pt	10	4	120	300	no heating	-
NR021	Si	10	2	60	300	pa 600 °C, 2 h, ppa 800 °C, 5h	175
NR022	Ti/Pt	10	2	60	300	pa 600 °C, 2 h	-
NR023	Si	8	2	60	300	no heating	165
NR024	Ti/Pt	8	2	60	300	no heating	-
NR025	Si	80	2	60	300	pa 700 °C, 2 h	-
NR026	Ti/Pt	80	2	60	300	pa 700 °C, 2 h	-
NR027	Si	100	2	60	300	no heating	-
NR028	Ti/Pt	100	2	60	300	no heating	300
NR029	Ti/Pt	10	4.2	120	300	no heating	-
NR030	Ti/Pt	10	4.2	120	310	no heating	-
NR031	Ti/Pt	30	4.2	120	300	no heating	-
NR032	Ti/Pt	30	4.2	120	300	no heating	-
NR033	Ti/Pt	30	4.2	120	300	no heating	-
NR034	Ti/Pt	12	4	120	270	heater broke down	-
NR035	Ti/Pt	15	4	120	300	TC 640 °C, P 350 °C	-
NR036	Ti/Pt	20	4	120	300	TC 792 °C, P 450 °C	-
NR037	Ti/Pt	20	4	120	300	TC 850 °C, P 500 °C	-
NR038	Ti/Pt	9	4	120	300	no heating	-
NR039	Ti/Pt	40	4	120	300	no heating	-
NR040	Ti/Pt	20	4	120	300	TC 890 °C, P 550 °C	-
NR041	Ti/Pt	20	4	120	300	TC 822 °C, P 520 °C	-
NR042	Ti/Pt	20	4	120	300	TC 938 °C, P 600 °C	-

LLTO reflexes as can be seen in Figure 4.15 for the latter sample.

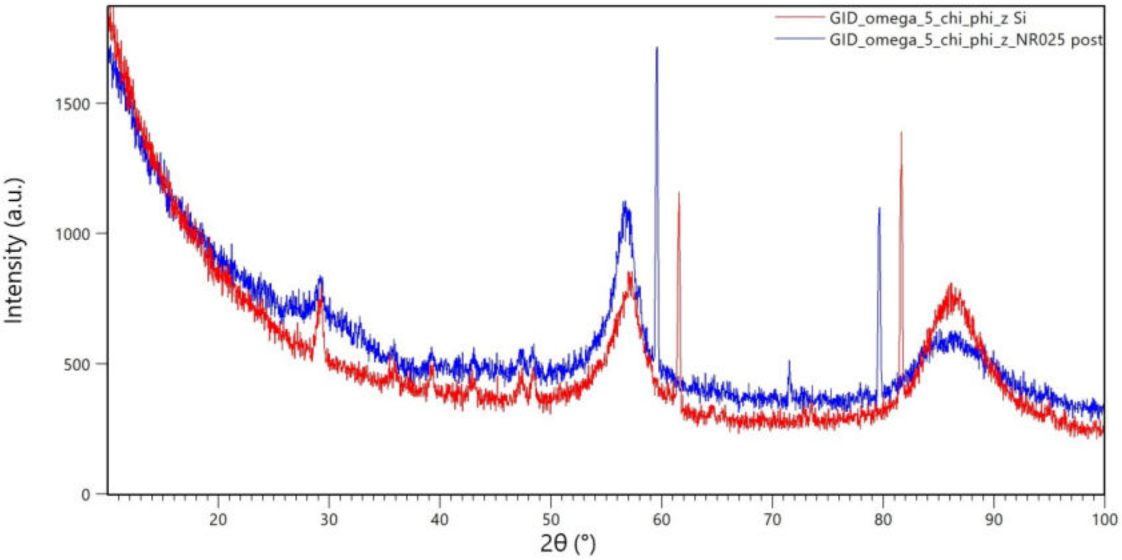

Figure 4.15: GID diffraction pattern: comparison of sample NR025 (blue, post-annealed at 700 °C for 2 h), and the silicon wafer as reference (red)

First LLTO reflexes appeared in sample NR036, which was heated to 450 °C during deposition. A combined GID diffractogram of the samples NR036 and NR037, heated to 500 °C during deposition, with the LLTO plate as reference (measured in GID mode, database reference code 04-011-8643, full diffractogram in Appendix) and the Ti/Pt layer on the sapphire substrate (reference diffractogram in Appendix, identified solely as Pt) is displayed in Figure 4.16.

The LLTO reflexes of the thin films are assigned to the reflexes of the LLTO reference plate respectively to the Pt substrate. Hereby, the most intense reflexes of the LLTO plate and the Pt background are compared to the reflexes of the samples. The results are presented in Table 4.8. The deviation of the sample reflexes to those of the LLTO plate is calculated in per cent.

The LLTO plate reflexes, which can be used for the sample assignment, are located at approx. 32°, 58° and 78° as here no Pt reflexes appear. Major overlaps occur at approx. 40°, 46°, 68° and 82°. The thin films do not exhibit all of the LLTO plate reflexes. This is most likely due to textured film growth. Furthermore, their reflexes are shifted in the majority to smaller angles in comparison to the LLTO plate. This indicates an expansion of the unit cell.

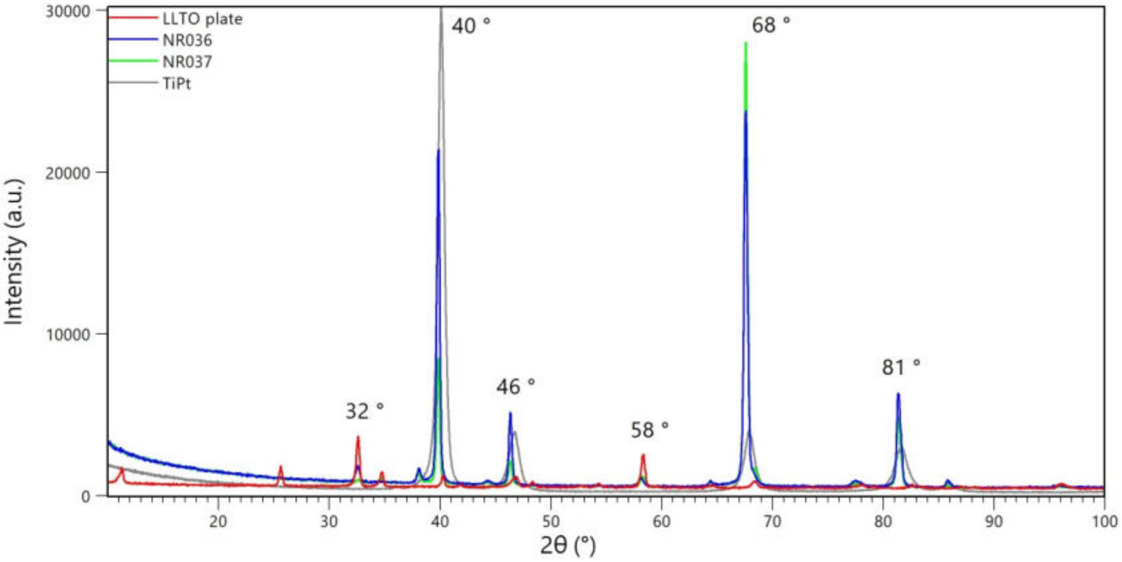

Figure 4.16: GID diffractogram: comparison of LLTO plate (red), sample NR036 (blue, deposition temperature 450 °C), sample NR037 (green, deposition temperature 500 °C) and Ti/Pt layer on a sapphire substrate (grey)

Table 4.8: LLTO thin film GID-XRD analysis: assignment of the thin film reflexes to the ones of the LLTO plate and the Pt background

LLTO plate (°2Θ)	Pt (°2Θ)	NR036 deviation (%)	NR037 to LLTO plate
11.2685	-	-	-
22.7880	-	-	-15.00
25.6175	-	-	-
32.5756	-	-0.09	0.49
34.8063	36.1461	-	-0.32
40.3070	40.1496	-1.13	-1.14
46.0237	46.7727	0.69	0.61
58.3671	-	-0.34	0.07
68.4185	67.8486	-1.28	-1.28
78.0573	-	-0.82	-0.95
82.5659	81.6055	-1.55	-1.54
83.4782	-	2.67	2.59
87.0671	86.0759	-	-
95.9888	-	-0.10	-0.03

In the standard measurement mode, the LLTO reflexes are harder to identify because the Pt signals are more intense. An example diffractogram is shown in Figure 4.17, the sample was deposited at 550 °C.

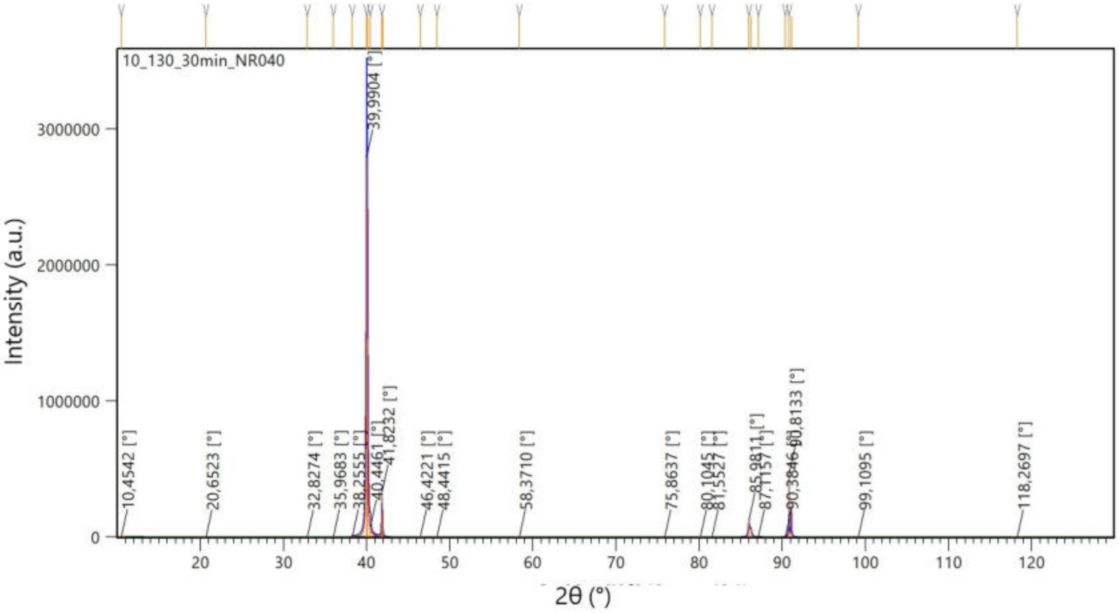

Figure 4.17: $\Theta - 2\Theta$ diffraction pattern: sample NR040, deposited at 550 °C with assigned reflex positions

Table 4.9: LLTO thin film XRD analysis, standard measurement mode: comparison of the reflex position of the thin films to the reflexes of the LLTO powder and Pt background

LLTO powder (°2Θ)	Pt (°2Θ)	NR035	NR036	NR037	NR040	NR042
		(deviation (%) to LLTO powder)				
11.3715	-	-	-	-	-	-
25.7206	-	-	-	-	-	-
32.6492	-	-1.25	-0.30	-0.61	0.36	-0.17
34.7618	-	-	-	-	-	2.68
-	37.5329	-	-	-	-	100
40.3034	39.8576	-1.58	-1.12	-1.63	-3.15	-1.43
-	41.684	-	-	-	-	-
46.971	46.7682	-1.77	-1.37	-1.74	-1.19	-1.56
58.3618	-	-0.90	-0.50	-0.29	0.11	-0.22
68.3611	-	-1.39	-0.05	-0.16	-1.02	-1.23
78.0815	-	-0.83	-	2.29	-	-
87.0961	86.025	-1.59	-1.46	-1.60	-1.30	-1.51
-	90.7241	-	-	-	-	-

The most intense reflex of the thin films, which can be assigned to the LLTO powder, appears at 86°. This reflex is shifted quite strongly in comparison to the LLTO powder. Nevertheless, it can be identified as an LLTO signal due to its unique shape. For a more detailed insight see diffractograms in Appendix (Figure 2 and 6). In the GID-XRD assignment of the thin film samples, the LLTO reflexes at 32° and 58° could be used. This is hardly possible in the standard XRD measurement mode as here almost no signal intensity can be observed. Furthermore, the reflex positions of the films are uniformly shifted to smaller angles in comparison to the LLTO powder. This was already discussed in the GID reflex assignment. Another point draws attention. The Pt reflex at 90° gets continuously smaller with the increase of the deposition temperature. One explanation would be that the Pt layer reacts with the LLTO film at higher temperatures and forms a new compound which has different diffraction reflexes.

4.4.1.1 In-situ post-annealing analysis

The analysis of the in-situ post-annealing diffractograms shows the transition from an amorphous to a crystalline film. More reflexes appear with the increase in temperature, however, they are very low in their intensity as the measurement was not performed in the GID setup. In Figure 4.18 an overview of measurement at different temperatures is shown.

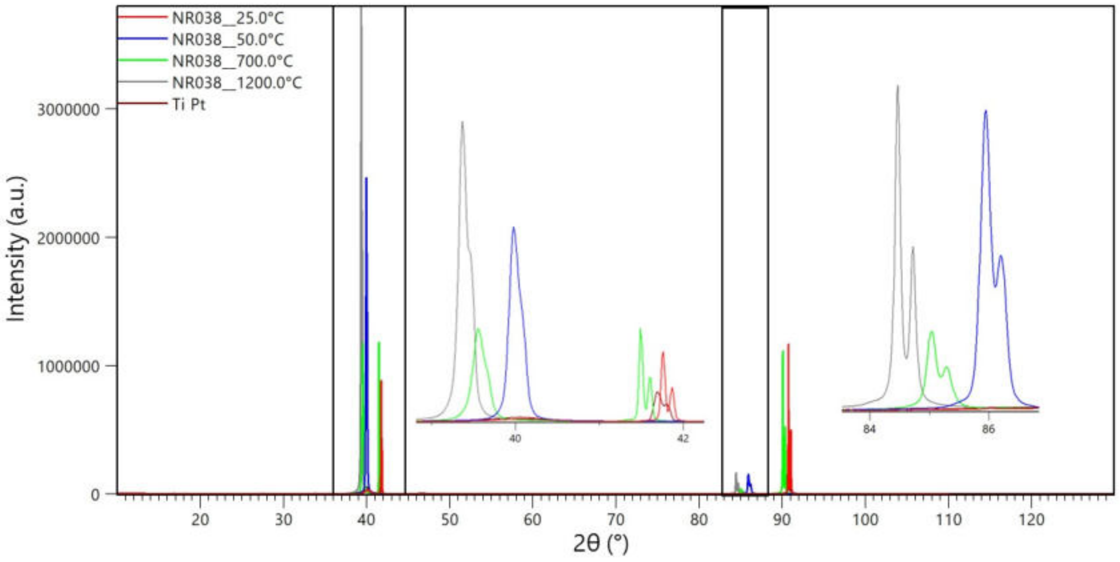

Figure 4.18: $\Theta - 2\Theta$ diffraction pattern: overview of in-situ post-annealing measurements; diffractogram at room temperature of 25 °C (red), 700 °C (green), 1200 °C (grey) and after cooling at 50 °C (blue), Ti/Pt layer on sapphire as reference (brown)

Various information can be derived. Firstly, the Pt reflex at 90° disappears at the high-temperature measurements and there is a reversal in the reflex intensities at the positions of 39.3° and 41.3°. The former increases with rising temperature, and the latter gets continuously smaller. Secondly, the characteristic LLTO reflex at approx. 86° appears within the heating, a first clear identification is possible at 500 °C. This reflex is shifted to larger angles as the sample is cooled down from 1200 °C to 50 °C due to the thermal relaxation of the lattice. After the measurements, the sample was completely discoloured.

In conclusion, crystalline LLTO films are obtained within hot sputtering at temperatures upon 350 °C. Sputtering at room temperature results in an amorphous structure. In the standard XRD setup, the most dominant LLTO sample reflex is located at 86°.

4.4.2 Chemical characterization of LLTO thin films

4.4.2.1 LA-ICP-MS and ICP-MS measurements

To obtain a more detailed chemical insight into the stoichiometry of the thin film samples, LA-ICP-MS and ICP-MS measurements were performed. As already mentioned in the LA-ICP-MS analysis of the targets, the obtained results are not usable in a quantitative way. The matrix effects for the thin films are even greater than for the targets, as here not only the layer itself but also the substrate will get depleted due to the small thickness. One interesting feature emerged from the measurements. The change in the film thickness of a sample, which is indicated in the variation of the Ti-46 signal, can be observed as line scans were performed. An example measurement is shown for sample NR001 in Figure 4.19. A more detailed film thickness discussion is given in subsection 4.4.3.

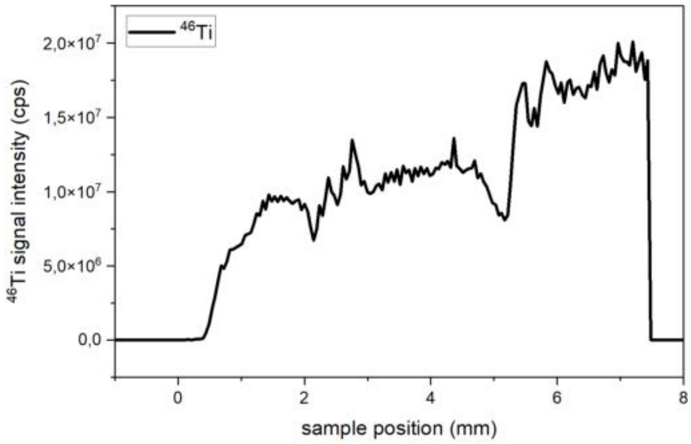

Figure 4.19: LA-ICP-MS line scan: surface scan of sample NR021 to observe the change in the signal intensity due to film thickness differences across the sample

The results from both, the LA-ICP-MS and ICP-MS, measurements are displayed in Table 4.10. The molar ratios were normalized to the titanium content to obtain molar compositions.

Table 4.10: LLTO thin film stoichiometric analysis: evaluation of LA-ICP-MS and ICP-MS results

sample	ICP-MS	ICP-MS: Li/La	LA-ICP-MS	LA-ICP: Li/La
NR001	$Li_{0.08}La_{0.56}TiO_3$	0.12	x	0.10
NR002	$Li_{0.08}La_{0.58}TiO_3$	0.14	x	0.15
NR003	$Li_{0.12}La_{1.04}TiO_3$	0.12	-	-
NR005	$Li_{0.01}La_{0.51}TiO_3$	0.01	-	-
NR007	$Li_{0.07}La_{0.52}TiO_3$	0.13	-	-
NR009	$Li_{0.01}La_{0.61}TiO_3$	0.01	x	0.01
NR017	$Li_{0.11}La_{0.54}TiO_3$	0.20	$Li_{0.15}La_{0.33}TiO_3$	0.45
NR019	x	0.30	-	-
NR021 pa	-	-	$Li_{0.29}La_{0.30}TiO_3$	0.97
NR022	x	0.16	-	-
NR023	$Li_{0.15}La_{0.53}TiO_3$	0.29	$Li_{0.25}La_{0.31}TiO_3$	0.81
NR025 pa	-	-	$Li_{0.45}La_{0.32}TiO_3$	1.41
NR027	$Li_{7.02}La_{0.61}TiO_3$	13.31	$Li_{40.87}La_{0.39}TiO_3$	104.79
NR035	x	0.12	-	-
NR040	x	0.03	-	-
ICP-MS, LLTO powder meas 1: $Li_{0.3}La_{0.57}TiO_3$, Li/La 0.54				
ICP-MS, LLTO powder meas 2: $Li_{0.3}La_{0.56}TiO_3$, Li/La 0.53				
manufacturer, LLTO powder: $Li_{0.3}La_{0.59}TiO_3$, Li/La 0.51				

It can be seen from the results table in Table 4.10 that the powder specification of the manufacturer corresponds well with the measurement results of the powder analysis. This confirms the chemical composition of the starting material.

The ICP-MS results of the samples NR001/2/3/5/9 have to be considered with caution as the samples were prepared with two dilution ratios, 1:10 and 1:50, which gave different results. Within the former, matrix effects may have influenced the measurement because the standards were prepared with a diluted HNO_3 solution and the thin films were dissolved in a concentrated HCl solution. In contrast, the measurements with the smaller dilution ratio had to deal with very low signals. Nevertheless, it was decided to take the results from the 1:50 ratio because of the more similar chemical environment.

The samples NR019/22/35/40 were sputtered on sapphire with a Ti/Pt layer, therefore only the Li/La ratio could be determined. The Li/La ratio of the LLTO powder amounts to 0.51. The thin films do not meet this specification, the samples NR019 (sputtered with 4 cm distance at 120 W) and NR023 (sputtered with 2 cm distance at 60 W) come closest to this value though.

Several problems occurred during the LA-ICP-MS measurement for the samples NR001/2/9, therefore only the Li/La ratio could be calculated. Generally, the LA-ICP-MS results are not quantitatively way due to the reported matrix effects. The highest, but unreasonably high, Li/La ratios are received with the samples NR021-NR027, which were sputtered with a distance of 2 cm. Furthermore, it can be seen that sample NR027, which was sputtered with $1 \cdot 10^{-1}$ mbar, exhibits an exorbitant amount of lithium. The further characterization of this sample will be discussed in later sections.

The effect of the vertical target to sample distance can be further evaluated within both techniques. The Li/La ratio of sample NR009, sputtered with 6.5 cm, is very low in comparison to the samples NR019, distance of 4 cm, or NR023, distance of 2 cm.
In addition, an effect through hot sputtering can be observed for samples NR035 and NR040. These samples were sputtered under almost the same conditions as sample NR019, however, their lithium content is considerably smaller. The lithium loss increases with higher temperatures.

For future experiments, over-stoichiometric targets could be tested, where an excess of lithium is used in the target material. This surplus could compensate for the loss of lithium during sputtering, resulting in a higher Li/La ratio in the thin film samples.

4.4.2.2 Further characterization methods

It was tried to analyze the samples with the methods of Raman spectroscopy and XRF analysis. Herein, bulk samples are required with a film thickness of at least 1 mm. The sputtered films, however, are only 100-300 nm thick.

The Raman measurements of the thin films did not work as only the silicon signal from the sample substrate was captured.
The XRF analysis provides very superficial qualitative information. A detailed analysis of the elemental composition could not be carried out due to the mentioned difficulties of low film thickness and missing calibration standards. Merely the presence of the elements La, Ti and O could be confirmed within the thin films.

4.4.3 Surface characterization of LLTO thin films

4.4.3.1 Film thickness measurements

The thickness of the sputtered films was measured with a profilometer. Hereby, the effect of the sputtering parameters on the film thickness is evaluated. Especially the vertical target to substrate distance is of high interest. However, it turned out that not only the vertical but also the horizontal distance from the sample substrate to the centre of the sputter gun is important. In Figure 4.20 the measured film thickness of some samples is depicted. The effect of the horizontal distance is analyzed for samples NR005 and NR007.

The side of the sample, which was closer to the sputter gun, is labelled with “near“, and the opposite side with “far“.

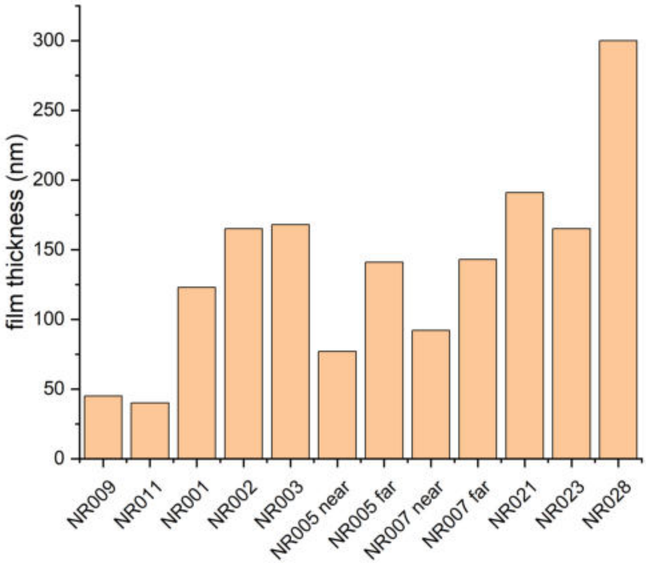

Figure 4.20: Film thickness analysis of the sputtered films via profilometer measurements

The results of samples NR005 and NR007 show a horizontal film thickness variation in the range of 100 nm. The colourful circular patterns on the sample surfaces are already indicating differences in thickness. Pictures of samples are shown in the Appendix, Figure 7 and 8. Furthermore, the effect of the vertical target to sample distance is evident when comparing samples NR001, NR011 and NR021 with a distance of 4.2, 6.5 and 2 cm. Sample NR011 displays the lowest value of these three measurements. Moreover, the impact of the pressure in the chamber could be experienced with the samples NR021 and NR028. The latter was sputtered with a ten times higher pressure, resulting in the largest measured thickness. This sample appeared very rough and it is the counterpart of sample NR027, which gave outstanding results due to its high lithium content in the stoichiometric analysis.

In sputtering not only the absolute film thickness but also the overall topology, including roughness and pinhole density, is an important factor. To investigate this property profilometer line scans over the surface of the samples were conducted as well as AFM and SEM measurements.

Two samples were especially interesting, sample NR021 and sample NR025, which were post-annealed after sputtering. Crystallite-shaped forms appeared after this procedure, which may be the result of a poor adhesion from the LLTO film on the silicon substrate, see Figure 4.21 and 4.22. Profilometer scans were conducted to measure the height difference between these crystallites and the substrate surface. Additionally, the samples NR028, sputtered at 2 cm with $1 \cdot 10^{-1}$ mbar, and NR035, deposited at 350 °C, were analyzed. The plots are shown in Figure 4.23 to 4.26.

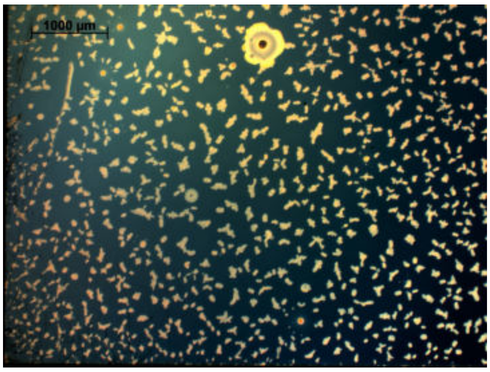

Figure 4.21: Optical microscope image: sample NR021, after post-annealing at 600 °C for 2 h

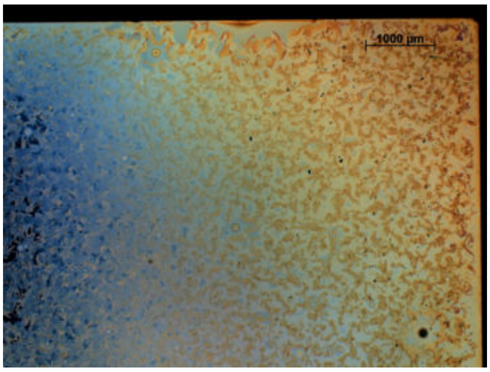

Figure 4.22: Optical microscope image: sample NR025, after post-annealing at 700 °C for 2 h

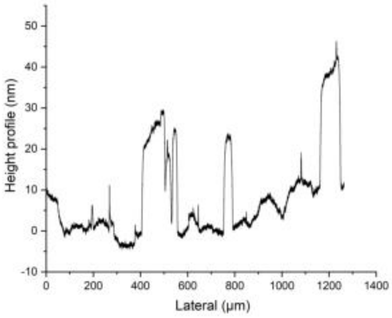

Figure 4.23: Profilometer line scan: NR021, after post-annealing at 600 °C for 2 h

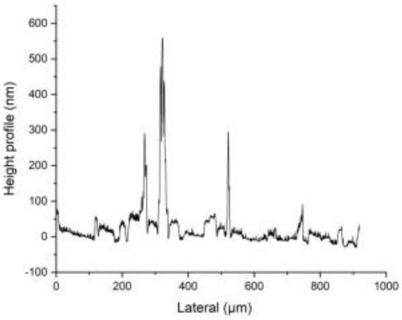

Figure 4.24: Profilometer line scan: sample NR025, after post-annealing at 700 °C for 2 h

The line scan of sample NR021 in Figure 4.23 displays that a clear distinction between the crystallites and the baseline can be drawn. However, this baseline is quite fluctuating and the height differences are only in the range of 30 nm. In addition, the distinction between crystallites and baseline is not evident for sample NR025. It is assumed that cavities are present in the thin films, which are responsible for the optical appearance of local "islands". The presence of real crystallites would be indicated through a larger height difference in the line scan.

The line scan from NR028 confirms the optical roughness as the height profile exhibits a lot of spikes. In contrast to this behaviour, sample NR035, a hot sputtered sample,

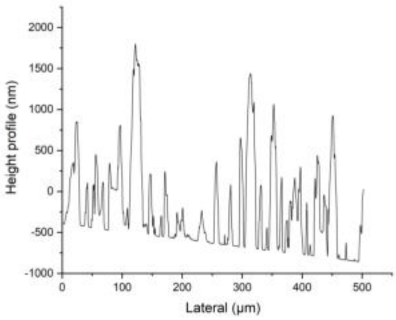

Figure 4.25: Profilometer line scan: sample NR028, sputtered at 2 cm with $1 \cdot 10^{-1}$ mbar

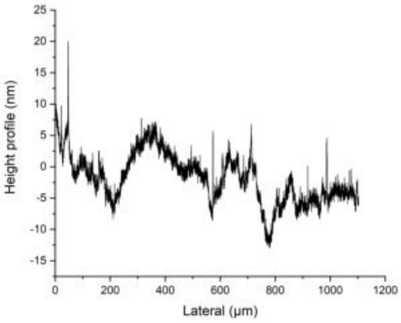

Figure 4.26: Profilometer line scan: sample NR035, deposited at 350 °C

displays a smooth surface.

4.4.3.2 AFM analysis

An additional topology analysis was carried out with atomic force microscopy measurements, the according graphs are depicted in Figure 4.27 to 4.30.

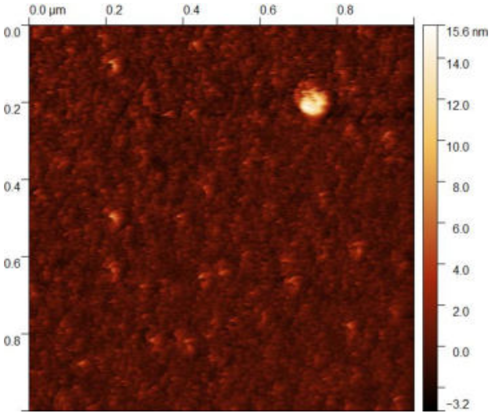

Figure 4.27: AFM image: sample NR021, after post-annealing at 600 °C for 2 h

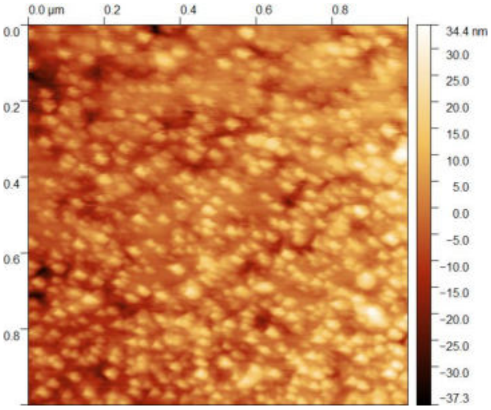

Figure 4.28: AFM image: sample NR028, sputtered at 2 cm with $1 \cdot 10^{-1}$ mbar

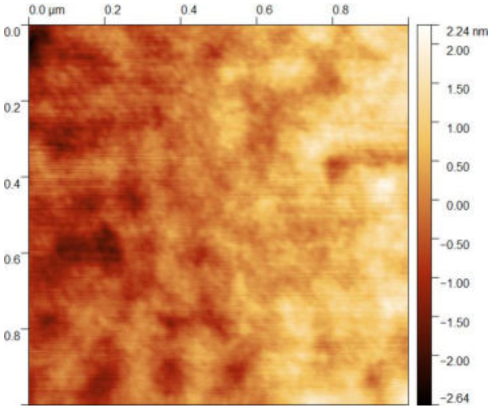

Figure 4.29: AFM image: sample NR031, sputtered at 4.2 cm with 120 W

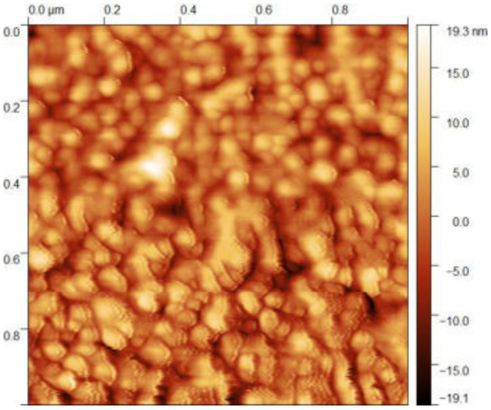

Figure 4.30: AFM image: sample NR035, hot sputtered at 4 cm with 120 W and 350 °C

The crystallite-shaped forms of the post-annealed sample NR021, which can be identified optically, can not be resolved metrologically by a difference in height to the substrate. This supports the theory that cavities are present and no crystallization process occurred. In general, all the measured samples exhibit a rather smooth surface. Even sample NR028, which showed rough features in the profilometer line scan, displays a flat surface. The limitation of AFM lies in the small measurement area and its resolution because this method is not intended to measure large height differences. Nevertheless, it can be stated that the samples display no major cracks or severe thickness fluctuations, which are favourable properties for sputtered thin films.

4.4.3.3 SEM analysis

Additional surface analysis was conducted using a scanning electron microscope. The taken micrographs are displayed in Figure 4.31 to 4.36.

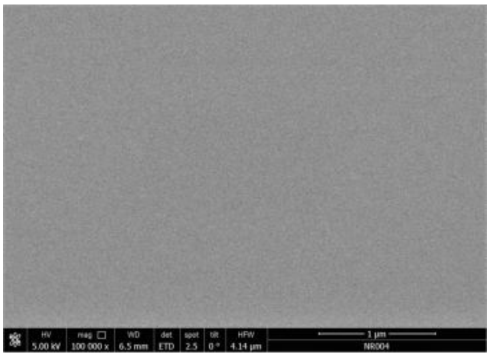

Figure 4.31: SEM image: sample NR004, sputtered at 4.2 cm with 120 W

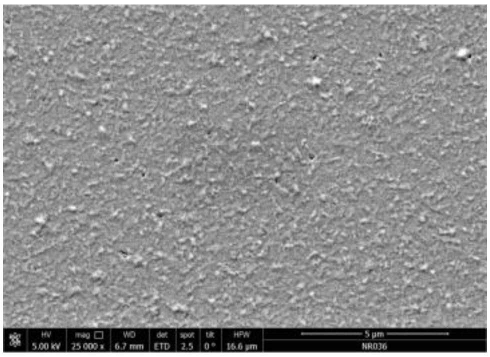

Figure 4.32: SEM image: sample NR036, hot sputtered at 4 cm with 120 W and 450 °C

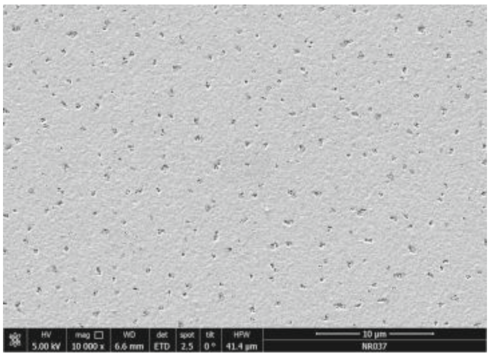

Figure 4.33: SEM image: sample NR037, hot sputtered at 4 cm with 120 W and 500 °C

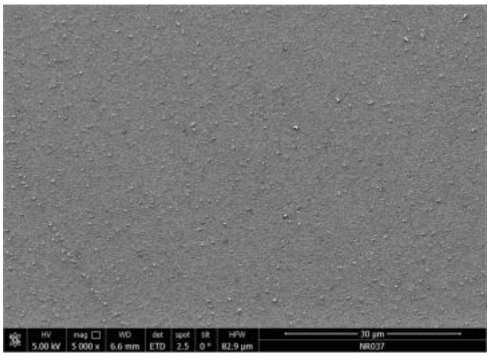

Figure 4.34: SEM image: sample NR037, hot sputtered at 4 cm with 120 W and 500 °C

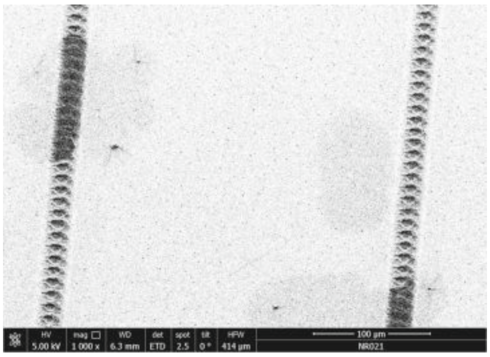

Figure 4.35: SEM image: sample NR021, after post-annealing at 600 °C for 2 h

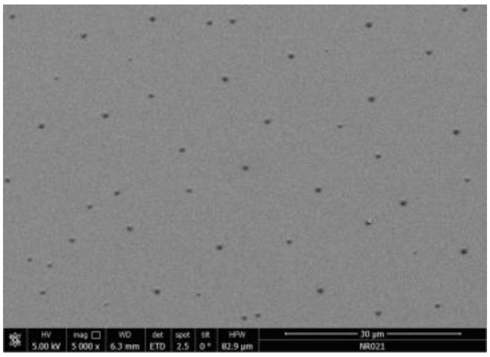

Figure 4.36: SEM image: sample NR021, after post-annealing at 600 °C for 2 h

Sample NR004, sputtered at 4.2 cm with 120 W, displays a very smooth surface with no pinholes or a specific structure. In contrast, the hot sputtered samples NR036, deposited at 450 °C, and NR037, deposited at 500 °C, do show a crystalline film structure. Pinholes and small particles can be seen as well, especially in sample NR037. A higher thermal load during sputtering could increase the pinhole density, which can also influence subsequent impedance measurements.
Furthermore, the focus is on the post-annealed sample NR021, which was already discussed in subsubsection 4.4.3.1 and 4.4.3.2. The supposed crystallites can be seen at very low magnification, indicating that no profound crystallite growth occurred. In addition, the surface seems to be overall flat with little black dots on it, which could not be identified.

In conclusion, the sputtered films display overall smooth surfaces with no major surface defects. The effects of the vertical and horizontal distances were evaluated. A height reduction in the vertical distance leads to an increased film thickness. The substrate should not be placed directly beneath the target to avoid horizontal thickness variations. The hot sputtered samples show crystalline patterns in the SEM micrographs.

4.4.4 Electrochemical characterization of LLTO thin films

Impedance spectra were recorded to obtain information about the electrochemical properties of the samples, in relation to the ionic conductivity and the capacitance. Microelectrodes, with a radius of 300 μm, were sputtered on the LLTO film for sample preparation, the sample structure is illustrated in Figure 3.1. However, most samples resulted in short-circuits. Pinholes in the thin films are probably mainly responsible for short-circuit measurements.

The first LLTO thin film samples were sputtered at room temperature which resulted in an amorphous structure. The hot sputtered samples exhibit a crystalline structure, hence, grain and grain boundary features are expected in the Nyquist plot. Pinholes are additionally detected with SEM measurements. It is therefore very likely that short-circuits appear. Due to the thin film nature of the samples, it is assumed that the grain and grain boundary semicircle can not be resolved as the latter probably interferes with the electrode feature. A single semicircle with a blocking electrode feature is expected, for both the amorphous and crystalline samples, as shown in Figure 2.4.

The plots were fitted with equivalent circuits in the software ZView. In general, it was difficult to obtain impedance spectra because, if at all, only a few microelectrodes of a sample were measurable. In addition, most of these spectra do not show the expected blocking electrode feature. Instead, semicircles are present which meet the real axis at low frequencies. Herein, a single R/CPE circuit is chosen for modelling. The exception is sample NR028, which is the counterpart to sample NR027 and has an exorbitant lithium content. Sample NR028 can be modelled with a R/CPE+CPE equivalent circuit. In Figure 4.37 and 4.38, two Nyquist plots are shown, for the amorphous sample NR010 and the hot sputtered sample NR036. A combined Nyquist plot of sample NR016 is shown in illustrated to Figure 4.39, to visualize the variance in the measurements.

In Table 4.11 the results of the impedance measurements are summarised, where the means for the conductivity and capacitance, according to Equation 2.9 and 2.10, are calculated. The thickness of the electrolyte film was generally set to 150 nm, except for sample NR028 with a thickness of 300 nm, the radius of the microelectrode is 300 μm. The theoretical bulk capacitance for a 150 nm thin film is determined with Equation 2.11, resulting in a value of $2.50 \cdot 10^{-9}$ F.

Electronic conductivity is indicated by the semicircles intersecting the x-axis. Furthermore, it can be seen that the sizes of the semicircles, and therefore the electronic conductivity, vary greatly between and within a single sample. This behaviour can be observed

Table 4.11: Results of LLTO thin film impedance measurements

sample	σ (S/cm)	C (F)
NR004 pa	$9.82 \cdot 10^{-6}$	$1.72 \cdot 10^{-10}$
NR010	$4.80 \cdot 10^{-5}$	$1.47 \cdot 10^{-9}$
NR012 pa	$6.68 \cdot 10^{-9}$	$4.64 \cdot 10^{-12}$
NR014 pa	$3.91 \cdot 10^{-5}$	$2.60 \cdot 10^{-9}$
NR016	$2.34 \cdot 10^{-5}$ to $4.97 \cdot 10^{-11}$	$1.29 \cdot 10^{-9}$
NR028	$1.83 \cdot 10^{-6}$	$2.04 \cdot 10^{-9}$
NR031	$3.66 \cdot 10^{-5}$	$1.02 \cdot 10^{-9}$
NR036	$1.77 \cdot 10^{-6}$	$3.23 \cdot 10^{-9}$
NR042	$6.63 \cdot 10^{-8}$	$3.44 \cdot 10^{-10}$

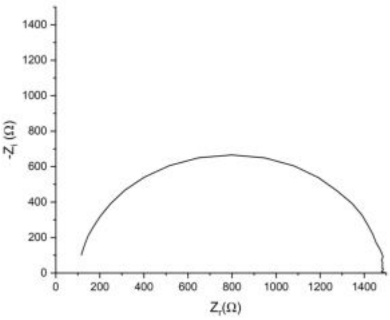

Figure 4.37: Nyquist plot: sample NR010, sputtered at 6.5 cm with 120 W

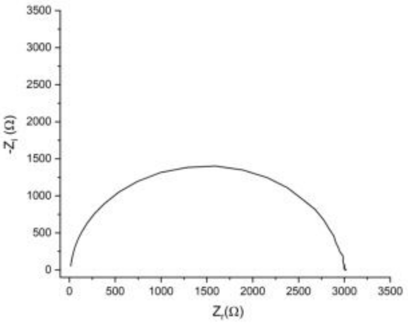

Figure 4.38: Nyquist plot: sample NR036, hot sputtered at 4 cm with 120 W at 450 °C

specifically in sample NR016. The reason for this variation lies in the measurement of different microelectrodes. Hereby, the material properties are influenced by the film quality, which is most likely affected by the horizontal sample distance, and local chemical composition as defect concentration.

The spectra do also show truncated semicircles with an additional offset. These plots are not discussed in detail since only speculations about the origin can be made. It is possible, though, that pinholes in the current path are responsible for these spectra.

It was assumed that the hot sputtered samples would result in more useable Nyquist plots because of their crystalline structure. However, this was not the case as the samples showed the same difficulties in the measuring process as the amorphous samples. As expected, no bulk and grain boundary semicircles could be resolved.

The capacitance of the samples is mostly in a range between 10^{-9} and 10^{-10} F. These are plausible values for the bulk capacitance of the material. The calculated capacitance from sample NR012 pa (post-annealed) is very low and probably comes from a contact resistance. Moreover, the shape of the obtained semicircles is another indicator of the presence of bulk capacitance.

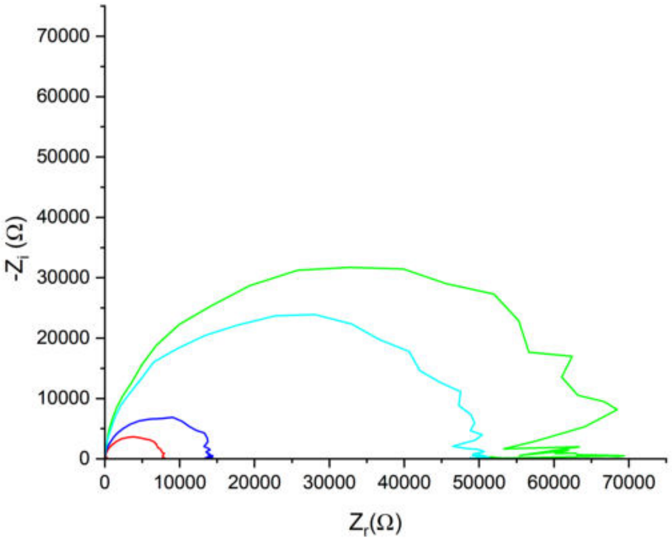

Figure 4.39: Nyquist plot: overview over different sized semicircles of sample NR016, sputtered at 6.5 cm with 140 W

The only sample which does exhibit the pattern of the expected equivalent circuit, shown in Figure 2.4, is sample NR028. An example of a Nyquist plot is displayed in Figure 4.40. Hence, the resistance of the high-frequency arc is attributed to the ionic conductivity.

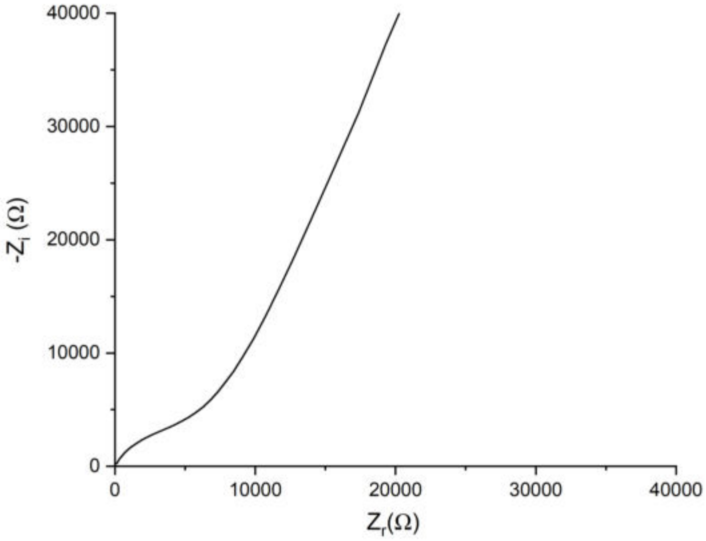

Figure 4.40: Nyquist plot: sample NR028, sputtered at 2 cm with $1 \cdot 10^{-1}$ mbar

To investigate the temperature effect on the ionic conductivity, a measurement series for sample NR028 was conducted, where impedance spectra were recorded at different temperatures, namely at 40 °C, 60 °C, 80 °C, 100 °C, 120 °C and 400 °C. The ionic conductivities are calculated for each temperature, the results are visualized in Figure 4.41.

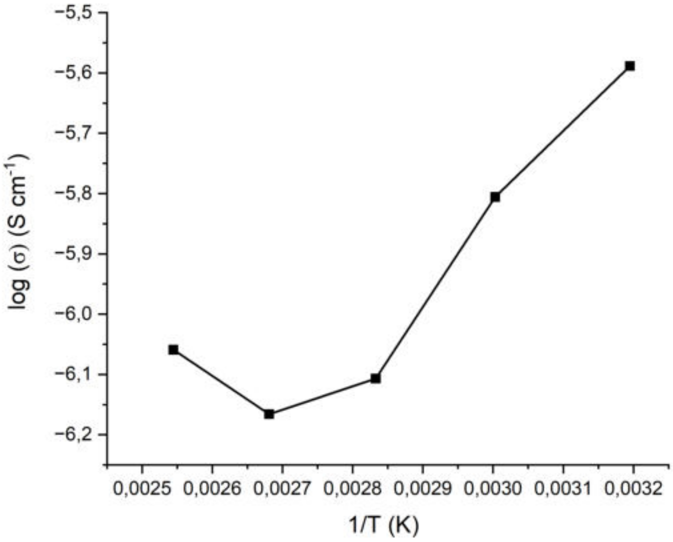

Figure 4.41: Arrhenius plot of sample NR028 after the temperature dependent measurements

It is expected for an electrolyte that the ionic conductivity increases with increasing temperature. This is not the case for sample NR028 as the conductivity values decrease with increasing temperature, an exception is the last data point at 400 °C, which marks the overall highest conductivity value. Additionally, the shape of the recorded spectrum changed at this temperature to a distorted semicircle, which does not intercept the x-axis. An explanation for the increased conductivity behaviour at the high temperature is that the film may have crystallized during heating, which improved the conductivity. It was further experienced that the sample heating had a detrimental effect as after the measurement series no usable Nyquist plots could be recorded.

In summary, sample NR028 provided the most reproducible Nyquist plots among all the samples measured. Due to its chemical composition, it is surprising that such results were obtained in this particular sample. The ICP-MS analysis resulted in a stoichiometry of $Li_{7.2}La_{0.61}TiO_3$, see results of sample NR027, which was sputtered under the same conditions. This composition deviates from the aimed stoichiometry of the LLTO powder. The surface appeared very rough in the profilometer line scans and the XRD measurements showed no signs of crystallinity. It is assumed that the high lithium content leads to relatively high conductivity. The behaviour in the Arrhenius experiment could be explained with regard to the formation of another lithium oxygen compound during sputtering. This phase could exhibit different chemical and electrochemical properties in comparison to LLTO.

The other samples displayed semicircles in the Nyquist plot, where varying conductivity values in the range of $4.97 \cdot 10^{-11}$ to $4.80 \cdot 10^{-5}$ S.cm^{-1} were obtained. The calculated capacitance values can be assigned to the bulk capacitance.

Chapter 5

Summary

In the course of this thesis, LLTO targets were successfully manufactured. Optimization of the sintering program resulted in pellets that had a flat structure and appeared visually dense. The favourable sintering settings included a sintering temperature of 1100 °C, a sintering time of 8h and an applied temperature ramp of 10 °Cmin^{-1}. The bonded targets were overall mechanically and thermally stable and the bonding layer did not dissolve during sputtering. However, it occurred that the edges of the targets broke due to the mechanical stress caused by the target bracket.
The target characterization techniques included XRD, RFA, Raman and ICP-MS measurements, where the former contributed most to the structural identification. The samples could be identified as pure LLTO. In the ICP-MS measurements, higher Li/La ratios were obtained for the LLTO target than for the LLTO powder.

Not only LLTO targets, but also Li_3PO_4 targets were produced. The optically densest target was achieved with a sintering temperature of 750 °C, a sintering time of 8 h and a temperature holding step at 500 °C. The structural identification with XRD measurements revealed that the targets crystallized in the γ-phase.
These targets were not used for sputtering LIPON thin films as the general conditions for the sputtering machine, regarding the required vacuum, were not given.

The major goal of the thesis was to sputter solid electrolyte LLTO thin films with self-produced LLTO targets. The thickness of the sputtered thin films was in the range of 100 to 300 nm. The elemental analysis was carried out with ICP-MS measurements. Herein, the lithium content was considerably smaller than in the LLTO powder. The best results were obtained with samples NR019, sputtered at 4 cm with 120 W, and NR023, sputtered at 2 cm with 60 W. Moreover, hot sputtering led to a decrease in the lithium content. In general, further optimization work with regard to the stoichiometric composition is necessary. Additionally, over-stoichiometric targets could be implemented for further experiments.

Crystalline films were obtained with hot sputtering at temperatures above 350 °C. The samples sputtered at room temperature had a uniform amorphous structure.
The thin films displayed a smooth surface structure with no major defects. Within the SEM analysis, crystalline patterns in the hot sputtered samples could be identified.
The electrochemical analysis was carried out with impedance measurements in a cross-plane setup. From theoretical considerations, an equivalent circuit consisting of a parallel series of a resistor and a constant phase element in series with a constant phase element, which indicates the blocking electrode system, should be present. However, most samples resulted in short-circuits. Some displayed a single, the x-axis intersecting semicircle in the Nyquist plot. This indicates electronic conductivity. Herein, broad variations in the semicircle size and thus in the conductivity were obtained. This variation could be attributed to local differences in the film quality due to variations of composition and/or film thickness. Furthermore, the calculated capacitance can be assigned to the bulk capacitance.
The only sample which resulted in the assumed equivalent circuit was the amorphous and non-stoichiometric sample NR028.

The sputtering machine was additionally modified during the work. The most important upgrades included the introduction of the smaller sputter gun, where sputter targets with a diameter of 2.54 cm could be used, and the height reduction of the recipient to enable hot sputtering.
Furthermore, the effect of the sputtering parameters, regarding plasma power, chamber pressure and vertical target to sample distance, were investigated. No film growth could be observed directly beneath the centre of the target, resulting from the formation of race track zones. This effect grew bigger with increasing distance, where a distance of 6.5 cm marked the threshold. Samples sputtered at this height had low film thicknesses and small Li/La ratios. However, a very small distance in combination with high pressure led to a rough surface with a very high lithium content.

Appendix

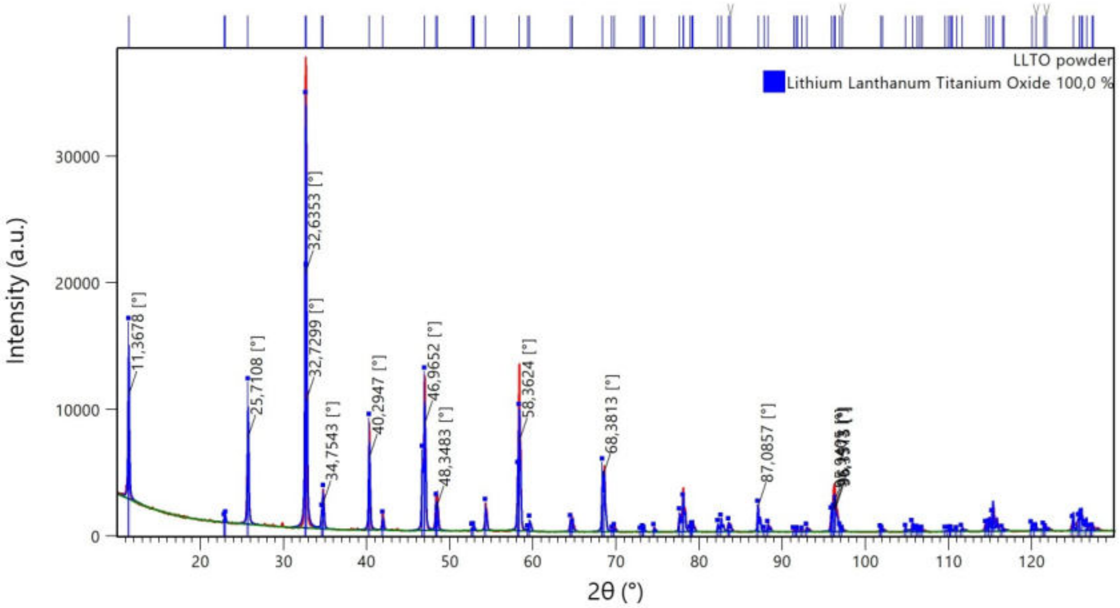

Figure 1: $\Theta - 2\Theta$ diffraction pattern: LLTO powder with reference file 04-020-7088

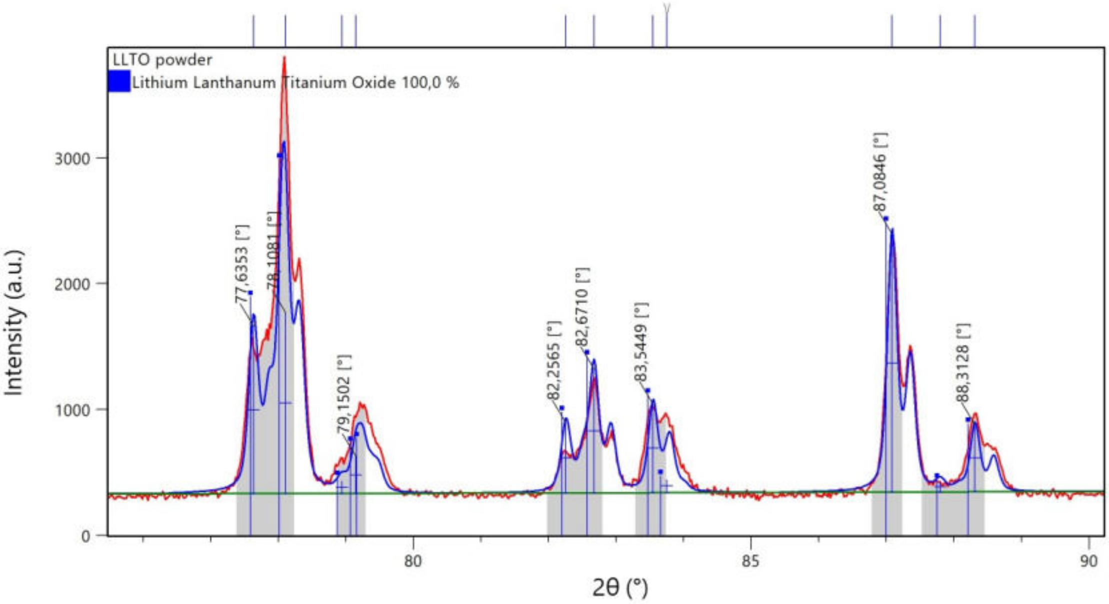

Figure 2: $\Theta - 2\Theta$ diffraction pattern: zoom into LLTO powder pattern at 86°, with assigned reference file

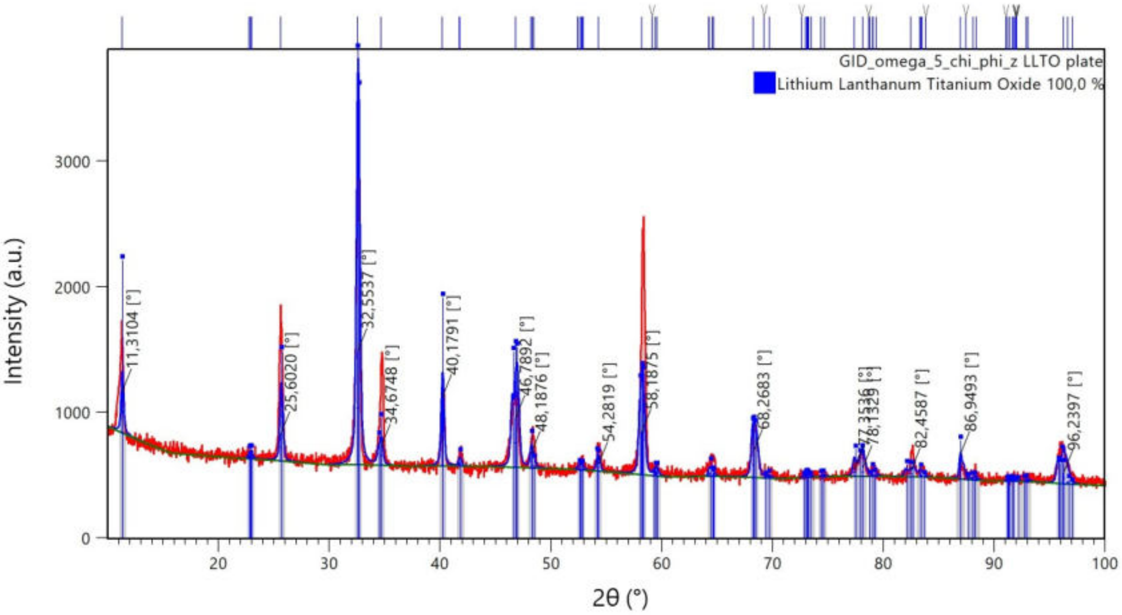

Figure 3: GID diffraction pattern: LLTO plate with reference file 04-011-8643

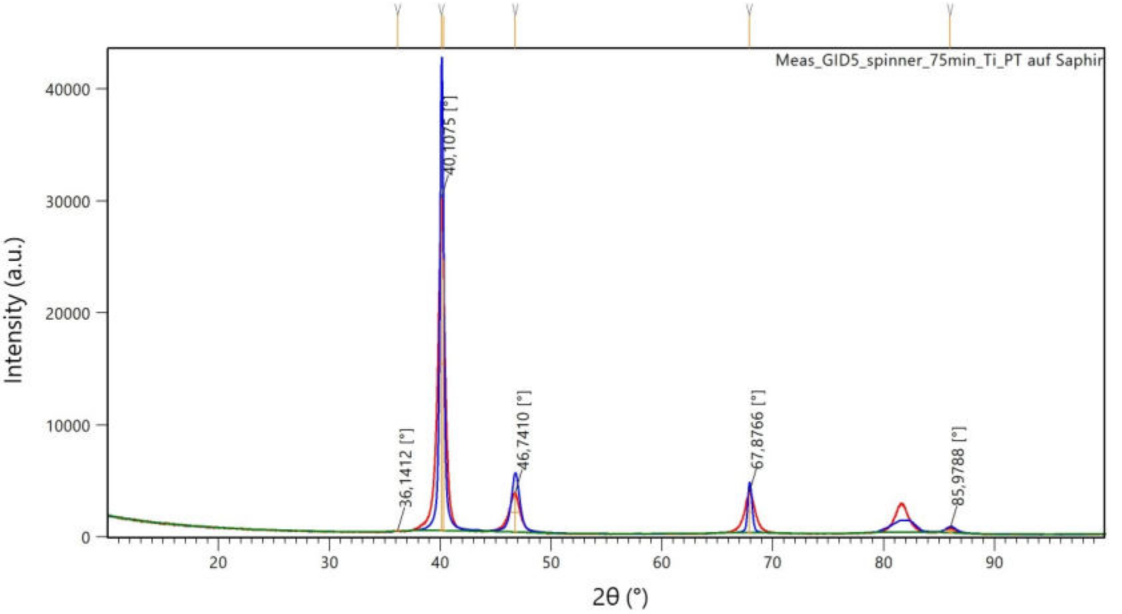

Figure 4: GID diffraction pattern: Ti/Pt layer on sapphire

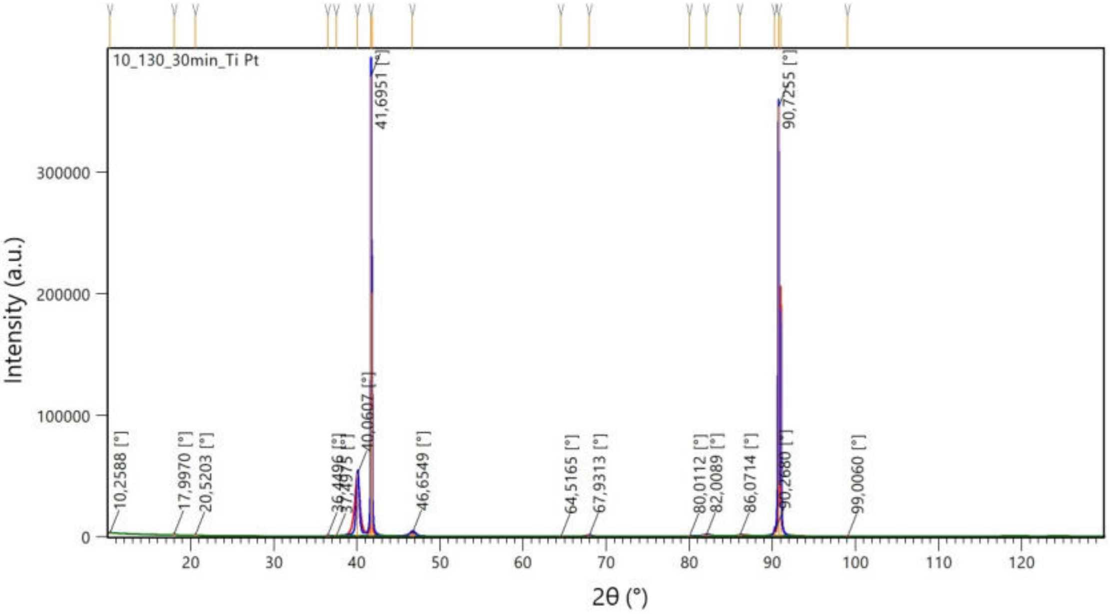

Figure 5: $\Theta - 2\Theta$ diffraction pattern: Ti/Pt layer on sapphire

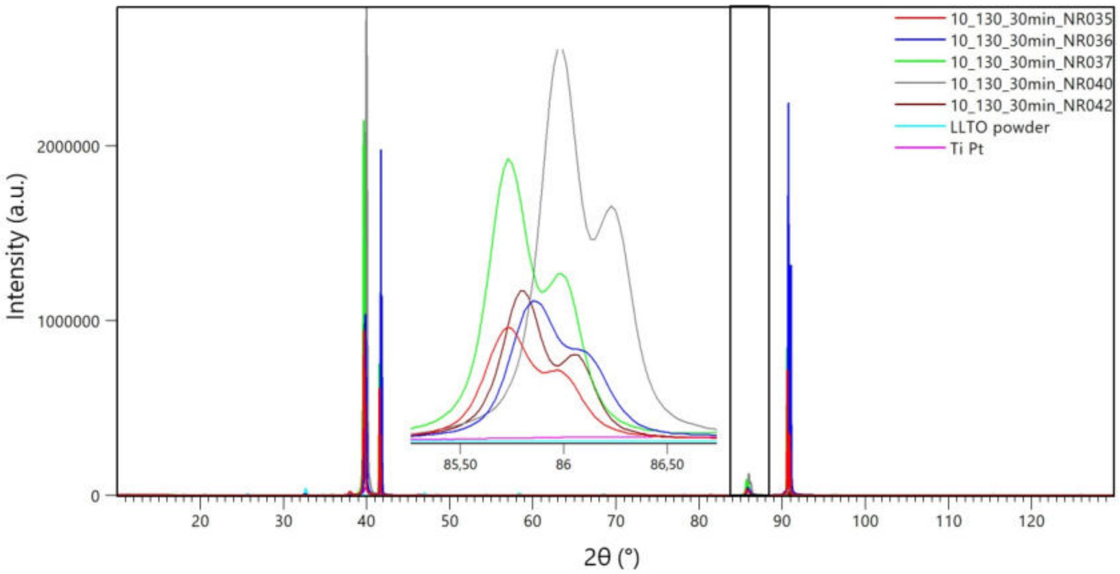

Figure 6: $\Theta - 2\Theta$ diffraction pattern: combined LLTO powder and LLTO thin film diffractogramm, colour code: sample NR035 (red), NR036 (dark blue), NR037 (green), NR040 (grey), NR042 (brown), LLTO powder (light blue) and Pt background (pink)

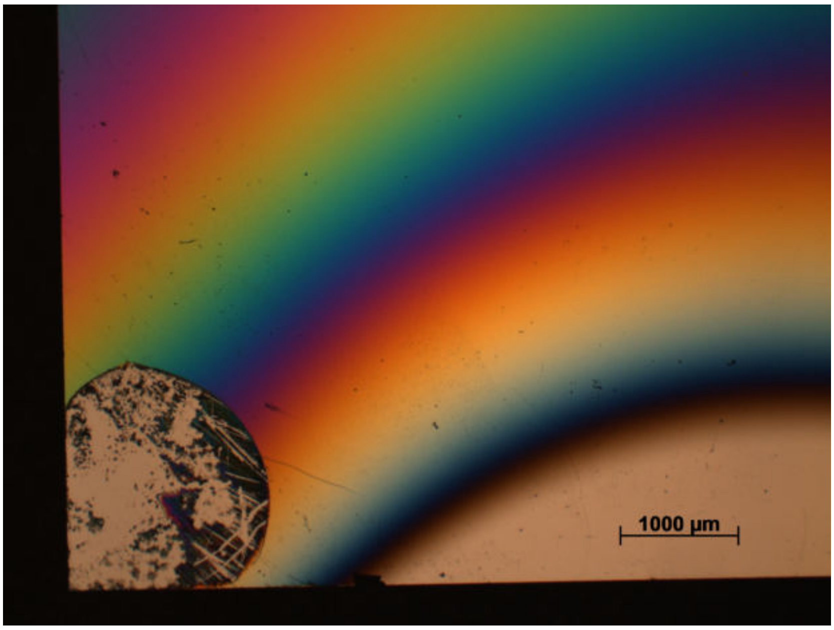

Figure 7: Microscope image: sample NR003, lower side closer to the sputter gun, sputtered at 4.2 cm with 120 W and $3 \cdot 10^{-2}$ mbar

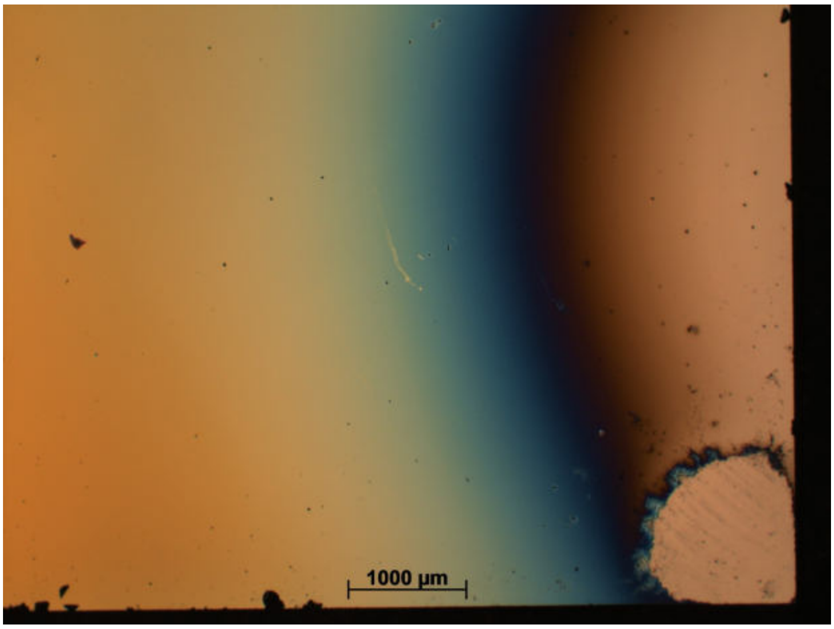

Figure 8: Microscope image: sample NR005, right side closer to the sputter gun, sputtered at 4.2 cm with 120 W $7 \cdot 10^{-3}$ mbar

Bibliography

[1] I. Dincer, “Renewable energy and sustainable development: A crucial review”, *Renewable and Sustainable Energy Reviews* **2000**, *4*, 157–175.

[2] C. Liu, F. Li, L.-P. Ma, H.-M. Cheng, “Advanced Materials for Energy Storage”, *Advanced Materials* **2010**, *22*, E28–E62.

[3] G. L. Soloveichik, “Battery Technologies for Large-Scale Stationary Energy Storage”, *Annual Review of Chemical and Biomolecular Engineering* **2011**, *2*, PMID: 22432629, 503–527.

[4] A. Nasiri, “Integrating energy storage with renewable energy systems”, **2008**, 17–18.

[5] H. Chen, T. N. Cong, W. Yang, C. Tan, Y. Li, Y. Ding, “Progress in electrical energy storage system: A critical review”, *Progress in Natural Science* **2009**, *19*, 294.

[6] Climate change and batteries: the search for future power storage solutions, The Royal Society, https://royalsociety.org/-/media/policy/projects/climate-change-science-solutions/climate-science-solutions-batteries.pdf.

[7] Ultracapacitor Frequently Asked Questions, Tecate Group, https://www.tecategroup.com/products/ultracapacitors/ultracapacitor-FAQ.php.

[8] Y. Wang, B. Liu, Q. Li, S. Cartmell, S. Ferrara, Z. Deng, J. Xiao, “Lithium and lithium ion batteries for applications in microelectronic devices: A review”, *Journal of Power Sources* **2015**, *286*, 330–345.

[9] M. Hu, X. Pang, Z. Zhou, “Recent progress in high-voltage lithium ion batteries”, *Journal of Power Sources* **2013**, *237*, 229–242.

[10] N. Nitta, F. Wu, J. T. Lee, G. Yushin, “Li-ion battery materials: present and future”, *Materials Today* **2015**, *18*, 252–264.

[11] W. Xu, J. Wang, F. Ding, X. Chen, E. Nasybulin, Y. Zhang, J.-G. Zhang, “Lithium metal anodes for rechargeable batteries”, *Energy Environ. Sci.* **2014**, *7*, 513–537.

[12] Q. Wang, P. Ping, X. Zhao, C. Guanquan, J. Sun, C. Chen, “ChemInform Abstract: Thermal Runaway Caused Fire and Explosion of Lithium Ion Battery”, *Journal of Power Sources* **2012**, *208*, 210–224.

[13] K. Xu, “Nonaqueous Liquid Electrolytes for Lithium-Based Rechargeable Batteries”, *Chemical Reviews* **2004**, *104*, 4303–417.

[14] J. Wen, Y. Yu, C. Chen, “A Review on Lithium-Ion Batteries Safety Issues: Existing Problems and Possible Solutions”, *Materials Express* **2012**, *2*, 197–212.

[15] S. K. Heiskanen, J. Kim, B. L. Lucht, “Generation and Evolution of the Solid Electrolyte Interphase of Lithium-Ion Batteries”, *Joule* **2019**, *3*, 2322–2333.

[16] A. Wang, S. Kadam, H. Li, S. Shi, Y. Qi, “Review on modeling of the anode solid electrolyte interphase (SEI) for lithium-ion batteries”, *npj Computational Materials* **2018**, *4*, 1–26.

[17] S. B. Peterson, J. Apt, J. Whitacre, “Lithium-ion battery cell degradation resulting from realistic vehicle and vehicle-to-grid utilization”, *Journal of Power Sources* **2010**, *195*, 2385–2392.

[18] J. Kim, B. Son, S. Mukherjee, N. Schuppert, A. Bates, O. Kwon, M. Choi, H. Chung, S. Park, “A review of lithium and non-lithium based solid state batteries”, *Journal of Power Sources* **2015**, *282*, 299–322.

[19] F. Zheng, M. Kotobuki, S. Song, M. O. Lai, L. Lu, “Review on solid electrolytes for all-solid-state lithium-ion batteries”, *Journal of Power Sources* **2018**, *389*, 198–213.

[20] J. Lau, R. DeBlock, D. Butts, D. Ashby, C. Choi, B. Dunn, “Sulfide Solid Electrolytes for Lithium Battery Applications”, *Advanced Energy Materials* **2018**, *8*, 1800933.

[21] E. Hayakawa, H. Nakamura, S. Ohsaki, S. Watano, “Characterization of solid-electrolyte/active-material composite particles with different surface morphologies for all-solid-state batteries”, *Advanced Powder Technology* **2022**, *33*, 103470.

[22] S. K. Sharma, G. Sharma, A. Gaur, A. Arya, F. S. Mirsafi, R. Abolhassani, H.-G. Rubahn, J.-S. Yu, Y. K. Mishra, “Progress in electrode and electrolyte materials: path to all-solid-state Li-ion batteries”, *Energy Adv.* **2022**, *1*, 457–510.

[23] Y. Zhang, Z. Zheng, X. Liu, M. Chi, Y. Wang, “Fundamental Relationship of Microstructure and Ionic Conductivity of Amorphous LLTO as Solid Electrolyte Material”, *Journal of The Electrochemical Society* **2019**, *166*, A515–A520.

[24] T. Teranishi, Y. Ishii, H. Hayashi, A. Kishimoto, “Lithium ion conductivity of oriented Li0.33La0.56TiO3 solid electrolyte films prepared by a sol–gel process”, *Solid State Ionics* **2016**, *284*, 1–6.

[25] Y. Hamedi Jouybari, F. Schmitz, “The influence of sputter conditions on the properties of LiPON and its interfaces”, *Journal of Power Sources* **2018**, *394*, 160–169.

[26] J. Schwenzel, V. Thangadurai, W. Weppner, “Developments of high-voltage all-solid-state thin-film lithium ion batteries”, *Journal of Power Sources* **2006**, *154*, 232–238.

[27] A. Jetybayeva, B. Uzakbaiuly, A. Mukanova, S.-T. Myung, Z. Bakenov, “Recent advancements in solid electrolytes integrated into all-solid-state 2D and 3D lithium-ion microbatteries”, *J. Mater. Chem. A* **2021**, *9*, 15140–15178.

[28] N. Dudney, B. Neudecker, “Solid state thin-film lithium battery systems”, *Current Opinion in Solid State and Materials Science* **1999**, *4*, 479–482.

[29] F. Wohde, M. Balabajew, B. Roling, “Li+ Transference Numbers in Liquid Electrolytes Obtained by Very-Low-Frequency Impedance Spectroscopy at Variable Electrode Distances”, *Journal of The Electrochemical Society* **2016**, *163*, A714.

[30] J. W. Fergus, “Ceramic and polymeric solid electrolytes for lithium-ion batteries”, *Journal of Power Sources* **2010**, *195*, 4554–4569.

[31] W. J. Kwon, H. Kim, K.-N. Jung, W. Cho, S. H. Kim, J.-W. Lee, M.-S. Park, “Enhanced Li+ conduction in perovskite Li3x La2/3-x 1/3-2x TiO3 solid-electrolytes via microstructural engineering”, *J. Mater. Chem. A* **2017**, *5*, 6257–6262.

[32] Y. Meesala, A. Jena, H. Chang, R.-S. Liu, “Recent Advancements in Li-Ion Conductors for All-Solid-State Li-Ion Batteries”, *ACS energy letters* **2017**, *2*, 2734–2751.

[33] S. Yan, C.-H. Yim, V. Pankov, M. Bauer, E. Baranova, A. Weck, A. Merati, Y. Abu-Lebdeh, “Perovskite Solid-State Electrolytes for Lithium Metal Batteries”, *Batteries* **2021**, *7*, 75.

[34] J. Z. Lee, Z. Wang, H. L. Xin, T. A. Wynn, Y. S. Meng, “Amorphous Lithium Lanthanum Titanate for Solid-State Microbatteries”, *Journal of The Electrochemical Society* **2016**, *164*, A6268.

[35] C. Chen, K. Amine, “Ionic conductivity, lithium insertion and extraction of lanthanum lithium titanate”, *Solid State Ionics* **2001**, *144*, 51.

[36] I. Kokal, PhD thesis, Chemical Engineering and Chemistry, **2012**.

[37] J. Wu, L. Chen, T. Song, Z. Zou, G. Jian, W. Zhang, S. Shi, “A review on structural characteristics, lithium ion diffusion behavior and temperature dependence of conductivity in perovskite-type solid electrolyte Li3x La2/3-x TiO3”, *Functional Materials Letters* **2017**, *10*, 1730002.

[38] S. Song, C. Yang, C. Jiang, Y. Wu, R. Guo, H. Sun, J.-L. Yang, Y. Xiang, X. Zhang, "Increasing ionic conductivity in Li0.33La0.56TiO3 thin-films via optimization of processing atmosphere and temperature", *Rare Metals* **2021**, *41*, 179–188.

[39] J. LaCoste, A. Zakutayev, L. Fei, "A Review on Lithium Phosphorus Oxynitride", *The Journal of Physical Chemistry C* **2021**, *125*, 3651–3667.

[40] Y. Su, J. Falgenhauer, A. Polity, T. Leichtweiß, A. Kronenberger, J. Obel, S. Zhou, D. Schlettwein, J. Janek, B. Meyer, "LiPON thin films with high nitrogen content for application in lithium batteries and electrochromic devices prepared by RF magnetron sputtering", *Solid State Ionics* **2015**, *282*, 63–69.

[41] B. Put, P. Vereecken, J. Meersschaut, A. Sepulveda Marquez, A. Stesmans, "Electrical Characterization of Ultrathin RF-Sputtered LiPON Layers for Nanoscale Batteries", *ACS Applied Materials and Interfaces* **2016**, *8*, 7060–7069.

[42] V. Lacivita, A. Westover, A. Kercher, N. Phillip, G. Yang, G. Veith, G. Ceder, N. Dudney, "Resolving the Amorphous Structure of Lithium Phosphorus Oxynitride (Lipon)", *Journal of the American Chemical Society* **2018**, *140*, 11029–11038.

[43] A. Baptista, J. Porteiro, J. Míguez, G. Pinto, "Sputtering Physical Vapour Deposition (PVD) Coatings: A Critical Review on Process Improvement and Market Trend Demands", *Coatings* **2018**, *8*, 402.

[44] P. Kelly, R. Arnell, "Magnetron sputtering: a review of recent developments and applications", *Vacuum* **2000**, *56*, 159–172.

[45] D. K. Maurya, A. Sardarinejad, K. Alameh, "Recent Developments in R.F. Magnetron Sputtered Thin Films for pH Sensing Applications—An Overview", *Coatings* **2014**, *4*, 756–771.

[46] A. Palmero, E. Hattum, W. Arnoldbik, A. Vredenberg, F. Habraken, "Characterization of the plasma in a radio-frequency magnetron sputtering system", *Journal of Applied Physics* **2004**, *95*, 7611–7618.

[47] N. Dudney, J. Bates, R. Zuhr, C. Luck, J. Robertson, "Sputtering of lithium compounds for preparation of electrolyte thin films", *Solid State Ionics* **1992**, *53-56*, 655–661.

[48] F. Ciucci, "Modeling electrochemical impedance spectroscopy", *Current Opinion in Electrochemistry* **2019**, *13*, Fundamental and Theoretical Electrochemistry, Physical and Nanoelectrochemistry, 132–139.

[49] Basics of Electrochemical Impedance spectroscopy, Gamry Instruments, https://www.c3-analysentechnik.eu/downloads/applikationsberichte/gamry/5657-Application-Note-EIS.pdf.

[50] H. Magar, Y. Rabeay, R. Hassan, A. Mulchandani, "Electrochemical Impedance Spectroscopy (EIS): Principles, Construction, and Biosensing Applications", *Sensors* **2021**, *21*, 6578.

[51] J. Macdonald, W. Johnson, I. Raistrick, D. Franceschetti, N. Wagner, M. Mckubre, D. Macdonald, B. Sayers, N. Bonanos, B. Steele, E. Butler, W. Worell, M. Stromme, S. Malmgren, S. Sundaram, G. Engelhardt, Y. Barsukov, W. Pell, C. Roland, R. Eisenberg, *Impedance Spectroscopy: Theory, Experiment, and Applications, Third Edition*, **2018**.

[52] M. E. Orazem, B. Tribollet, *Electrochemical impedance spectroscopy*, Second edition., Wiley, Hoboken, New Jersey, **2017**.

[53] J. Fleig, "The Grain Boundary Impedance of Random Microstructures: Numerical Simulations and Implications for the Analysis of Experimental Data", *Solid State Ionics* **2002**, *150*, 181–193.

[54] P. Vadhva, J. Hu, M. J. Johnson, R. Stocker, M. Braglia, D. J. L. Brett, A. J. E. Rettie, "Electrochemical Impedance Spectroscopy for All-Solid-State Batteries: Theory, Methods and Future Outlook", *ChemElectroChem* **2021**, *8*, 1930–1947.

[55] X. Qian, N. Gu, Z. Cheng, X. Yang, E. Wang, S. Dong, "Methods to study the ionic conductivity of polymeric electrolytes using a.c. impedance spectroscopy", *Journal of Solid State Electrochemistry* **2001**, *6*, 8–15.

[56] T. Grove, M. Masters, R. Meirs, "Determining Dielectric Constants Using a Parallel Plate Capacitor", *Physics Faculty Publications* **2005**, *73*, 52–56.

[57] S. Wilschefski, M. Baxter, "Inductively Coupled Plasma Mass Spectrometry: Introduction to Analytical Aspects", *The Clinical biochemist. Reviews* **2019**, *40*, 115–133.

[58] B. Fernández, F. Claverie, C. Pécheyran, O. F. Donard, F. Claverie, "Direct analysis of solid samples by fs-LA-ICP-MS", *TrAC Trends in Analytical Chemistry* **2007**, *26*, 951–966.

[59] Grazing incidence x-ray diffraction, Measurlabs, https://measurlabs.com/methods/grazing-incidence-x-ray-diffraction-gixrd/.

[60] M. Catti, M. Sommariva, R. M. Ibberson, "Tetragonal superstructure and thermal history of Li0.3La0.567TiO3 (LLTO) solid electrolyte by neutron diffraction", *J. Mater. Chem.* **2007**, *17*, 1300–1307.

[61] M. Romero, R. Faccio, S. Vázquez, S. Davyt, Á. W. Mombrú, "Experimental and theoretical Raman study on the structure and microstructure of Li0.30La0.57TiO3 electrolyte prepared by the sol-gel method in acetic medium", *Ceramics International* **2016**, *42*, 15414–15422.

[62] A. Kezionis, E. Kazakevicius, S. Kazlauskas, A. Zalga, “Metal-like temperature dependent conductivity in fast Li+ ionic conductor Lithium Lanthanum Titanate”, *Solid State Ionics* **2019**, *342*, 115060.

[63] N. Ishigaki, J. Akimoto, “Room temperature synthesis and phase transformation of lithium phosphate Li3PO4 as solid electrolyte”, *Journal of Asian Ceramic Societies* **2021**, *9*, 452–458.